

## Article

# Abnormal $\text{Eu}^{3+} \rightarrow \text{Eu}^{2+}$ Reduction in $\text{Ca}_{9-x}\text{Mn}_x\text{Eu}(\text{PO}_4)_7$ Phosphors: Structure and Luminescent Properties

Elena V. Sipina <sup>1</sup>, Dmitry A. Spassky <sup>2,3</sup> , Nataliya R. Krutyak <sup>1,3</sup>, Vladimir A. Morozov <sup>4</sup> , Evgenia S. Zhukovskaya <sup>4</sup>, Alexei A. Belik <sup>5</sup> , Mikhail S. Manylov <sup>4</sup> , Bogdan I. Lazoryak <sup>4</sup> and Dina V. Deyneko <sup>4,6,\*</sup> 

<sup>1</sup> Physics Department, Lomonosov Moscow State University, 119991 Moscow, Russia

<sup>2</sup> Skobeltsyn Institute of Nuclear Physics, Lomonosov Moscow State University, 119991 Moscow, Russia

<sup>3</sup> Institute of Physics, University of Tartu, 50411 Tartu, Estonia

<sup>4</sup> Department of Chemistry, Lomonosov Moscow State University, 119991 Moscow, Russia

<sup>5</sup> International Center for Materials Nanoarchitectonics (WPI-MANA), National Institute for Materials Science (NIMS), Tsukuba 305-0044, Ibaraki, Japan

<sup>6</sup> Laboratory of Arctic Mineralogy and Material Sciences, Kola Science Centre, Russian Academy of Sciences, 184209 Apatity, Russia

\* Correspondence: deynekomsu@gmail.com

**Abstract:**  $\beta\text{-Ca}_3(\text{PO}_4)_2$ -type phosphors  $\text{Ca}_{9-x}\text{Mn}_x\text{Eu}(\text{PO}_4)_7$  have been synthesized by high-temperature solid-phase reactions. The crystal structure of  $\text{Ca}_8\text{MnEu}(\text{PO}_4)_7$  was characterized by synchrotron X-ray diffraction. The phase transitions, magnetic and photoluminescence (PL) properties were studied. The abnormal reduction  $\text{Eu}^{3+} \rightarrow \text{Eu}^{2+}$  in air was observed in  $\text{Ca}_{9-x}\text{Mn}_x\text{Eu}(\text{PO}_4)_7$  according to PL spectra study and confirmed by X-ray photoelectron spectroscopy (XPS).  $\text{Eu}^{3+}$  shows partial reduction and coexistence of  $\text{Eu}^{2+}/^{3+}$  states. It reflects in combination of a broad band from the  $\text{Eu}^{2+} 4f^65d^1 \rightarrow 4f^7$  transition and a series of sharp lines attributed to  $^5\text{D}_0 \rightarrow ^7\text{F}_j$  transitions of  $\text{Eu}^{3+}$ .  $\text{Eu}^{2+}/\text{Eu}^{3+}$  ions are redistributed among two crystal sites, M1 and M3, while  $\text{Mn}^{2+}$  fully occupies octahedral site M5 in  $\text{Ca}_8\text{MnEu}(\text{PO}_4)_7$ . The main emission band was attributed to the  $^5\text{D}_0 \rightarrow ^7\text{F}_2$  electric dipole transition of  $\text{Eu}^{3+}$  at 395 nm excitation. The abnormal quenching of  $\text{Eu}^{3+}$  emission was observed in  $\text{Ca}_{9-x}\text{Mn}_x\text{Eu}(\text{PO}_4)_7$  phosphors with doping of the host by  $\text{Mn}^{2+}$  ions. The phenomena of abnormal reduction and quenching were discussed in detail.

**Keywords:** TCP structure; whitlockite; phosphates; abnormal reduction; photoluminescence



**Citation:** Sipina, E.V.; Spassky, D.A.; Krutyak, N.R.; Morozov, V.A.; Zhukovskaya, E.S.; Belik, A.A.; Manylov, M.S.; Lazoryak, B.I.; Deyneko, D.V. Abnormal  $\text{Eu}^{3+} \rightarrow \text{Eu}^{2+}$  Reduction in  $\text{Ca}_{9-x}\text{Mn}_x\text{Eu}(\text{PO}_4)_7$  Phosphors: Structure and Luminescent Properties. *Materials* **2023**, *16*, 1383. <https://doi.org/10.3390/ma16041383>

Academic Editor: Toma Stoica

Received: 5 January 2023

Revised: 21 January 2023

Accepted: 3 February 2023

Published: 7 February 2023



**Copyright:** © 2023 by the authors. Licensee MDPI, Basel, Switzerland. This article is an open access article distributed under the terms and conditions of the Creative Commons Attribution (CC BY) license (<https://creativecommons.org/licenses/by/4.0/>).

## 1. Introduction

The global search for obtainable phosphors emitting in the red region of the spectrum continues to the present, due to the requirements for creating high-quality light from modern LED illuminators. The aims of red phosphors are to improve the color rendering (CRI) and lower the resulting correlated color temperature (CCT) of the LED package. The main requirements for such phosphors are:

- (1) A broad excitation band which can be matched well with the light from the LED chip (usually, at 450–470 nm from the InGaN chip). A number of  $\text{Eu}^{3+}$ -doped inorganic red phosphors have been developed with the narrow emission due to the electric dipole  $^5\text{D}_0 \rightarrow ^7\text{F}_2$  transition located at 610–630 nm. This transition is dominant in most hosts due to the noncentrosymmetric environment. However, such luminescent materials mismatch the excitation wavelengths from the LED chip since the main excitation band of the  $\text{Eu}^{3+}$  ion is located obviously at 392–396 nm and has a narrow character;
- (2) A narrow emission band in the red region (full width at half-maximum (FWHM) should not exceed 20 nm to reduce radiative losses in the near-IR range) [1]. Moreover, the barycenter of the emission band must not lie beyond 650 nm to minimize wasted emission [2];

- (3) A high stability in the environment and high luminous efficiency of radiation (LER). LER values increase with the narrowing of the emission line from red phosphor [1]. At the moment, the luminous efficiency from red phosphors can reach values of 54 lm/W (lumens per watt) [3].

Red-emitting phosphors that mostly meet the technological requirements can be created, for example, based on nitrides [4] or oxynitrides, such as  $(\text{Ba,Sr})_2\text{Si}_5\text{N}_8:\text{Eu}^{2+}$  [5],  $(\text{Ca,Sr})\text{SiAlN}_3:\text{Eu}^{2+}$  [6] or  $\text{Sr}[\text{Li}_2\text{Al}_2\text{O}_2\text{N}_2]:\text{Eu}^{2+}$  [7]. For obtaining such compositions, metal nitrides  $\text{Si}_3\text{N}_4$  and  $\text{AlN}$  are usually used as raw materials which are air-sensitive and require a combination of high temperatures (up to 1700 °C) with a reducing atmosphere [8].

Phosphors based on hexafluorometallates, such as  $\text{K}_2\text{SiF}_6:\text{Mn}^{4+}$  [9], for instance, satisfy the requirement to reduce the consumption of rare-earth elements [10] and emit an extremely narrow photoluminescence band (used to increase the brightness of displays) due to intra-configuration 3d-3d transitions of  $\text{Mn}^{4+}$  ions. However, high-cost Si sources and not environment-friendly hydrofluoric acid are used in the synthesis. Moreover, they are very sensitive to moisture in the air and have long decay times, which limit their application.

According to the above, phosphate-based phosphors are important luminescent materials due to their excellent stability and available synthesis conditions. At the same time, the incorporation of  $\text{Mn}^{2+}$  ions into the  $\beta\text{-Ca}_3(\text{PO}_4)_2$ -type ( $\beta\text{-TCP}$ ) structure phosphates makes it possible to both stabilize the crystal structure [11] and to obtain photoluminescent properties from  $\text{Mn}^{2+}$  ions [12]. The stabilization of the lattice occurs due to the reduction of geometric stress in the octahedral site during  $\text{Ca}^{2+} \rightarrow \text{Mn}^{2+}$  substitution since the ionic radii of  $\text{Mn}^{2+}$  ( $r_{\text{VI}} = 0.83 \text{ \AA}$ ) are less than  $\text{Ca}^{2+}$  ( $r_{\text{VI}} = 1.00 \text{ \AA}$ ).  $\text{Mn}^{2+}$ -doped phosphates show a broad emission band at 600–750 nm, peaked at 650 nm [12–14], which corresponds to the red region of the visible spectrum.  $\text{Mn}^{2+}$  ions, as an activator, show a wide emission band from the  ${}^4\text{T}_1({}^4\text{G}) \rightarrow {}^6\text{A}_1({}^6\text{S})$  transition in the PL spectrum [13]. This emission strongly depends on the crystal field and can shift from green to red color. In an octahedral environment with a strong crystal field,  $\text{Mn}^{2+}$  ions usually generate red emission. If  $\text{Mn}^{2+}$  ions are located in a tetrahedral environment with a weak crystal field, green emission could be observed [15,16]. A serious advantage of  $\text{Mn}^{2+}$  doping into the  $\beta\text{-TCP}$  structure is a strong absorption of excitation at 450–480 nm, which is matching with the InGaN blue chip [13].

Co-doping strategy using  $\text{Eu}^{2+}/\text{Mn}^{2+}$  [17] or  $\text{Ce}^{3+}/\text{Mn}^{2+}$  [18] ions can improve the emission intensity due to the energy transfer processes in comparison to single-doped  $\beta\text{-TCP}$ -type hosts. For the CIE color adjustment and white light production, the combinations of rare-earth ions with  $\text{Mn}^{2+}$  at different concentrations can be used, such as  $\text{Ce}^{3+}/\text{Tb}^{3+}/\text{Mn}^{2+}$  or  $\text{Eu}^{2+}/\text{Tb}^{3+}/\text{Mn}^{2+}$ . Moreover, there is a possibility to obtain  $\text{Mn}^{2+}$  to  $\text{Eu}^{3+}$  energy transfer for enhancement of red  $\text{Eu}^{3+}$  emission [15,19,20] while  $\text{Eu}^{2+}$  to  $\text{Mn}^{2+}$  energy transfer is commonly observed [21]. Some data on  $\text{Mn}^{2+}$  and RE/ $\text{Mn}^{2+}$  (RE—rare-earth element) doped  $\beta\text{-TCP}$  phosphors are summarized in Table 1.

The idea of the present research was to combine the emission from  $\text{Eu}^{3+}$  and  $\text{Mn}^{2+}$  ions in the stable and easily synthesized host to obtain ideal red phosphor. The structure's features were studied using synchrotron X-ray diffraction. The abnormal reduction of  $\text{Eu}^{3+}$  in air was observed according to PL spectra and confirmed by XPS data. Moreover, a strong quenching of  $\text{Eu}^{3+}$  emission was detected in  $\text{Ca}_{9-x}\text{Mn}_x\text{Eu}(\text{PO}_4)_7$ , which is the opposite to other  $\text{Ca}_{9-x}\text{M}_x\text{Eu}(\text{PO}_4)_7$  phosphates with divalent metals, such as  $\text{Mg}^{2+}$  or  $\text{Zn}^{2+}$ . The mechanisms of self-reduction and quenching are discussed in detail.

**Table 1.** The characteristics of PL spectra and some features of Mn<sup>2+</sup> or RE/Mn<sup>2+</sup>-doped β-TCP-type phosphors.

Host	RE/Mn <sup>2+</sup> Combination	PL Spectra (Band Location/Peak of the Band)	Features	Ref.
Ca <sub>9</sub> Mn <sub>1-x</sub> Na(PO <sub>4</sub> ) <sub>7</sub> :xM <sup>2+</sup> , M = Zn, Mn	Mn <sup>2+</sup> and Eu <sup>2+</sup> /Mn <sup>2+</sup>	600–750 nm/655 nm	The co-doping of Zn <sup>2+</sup> /Mg <sup>2+</sup> and Mn <sup>2+</sup> broke the intrinsic structural confinement of Mn <sup>2+</sup> and improved its red emission.	[13]
Sr <sub>19</sub> (Mg <sub>1-x</sub> Mn <sub>x</sub> ) <sub>2</sub> (PO <sub>4</sub> ) <sub>14</sub> :yEu <sup>2+</sup>	Eu <sup>2+</sup> /Mn <sup>2+</sup>	550–750 nm/610 nm	The emission bands were attributed to Eu <sup>2+</sup> and Mn <sup>2+</sup> in different sites.	[17]
Ca <sub>8</sub> MgGd(PO <sub>4</sub> ) <sub>7</sub> :Eu <sup>2+</sup> /Mn <sup>2+</sup>	Eu <sup>2+</sup> /Mn <sup>2+</sup>	600–750 nm/650 nm λ <sub>ex</sub> = 365 nm	Efficient Eu <sup>2+</sup> → Mn <sup>2+</sup> energy transfer was observed, Eu <sup>2+</sup> emission intensity decreased.	[22]
Ca <sub>9</sub> MMn(PO <sub>4</sub> ) <sub>7</sub> (M = Li, Na, K)	Mn <sup>2+</sup>	580–720 nm/645 nm	The excitation by β-source <sup>90</sup> Sr- <sup>90</sup> Y. Mn <sup>2+</sup> occupies M5 site, M <sup>+</sup> ions (Li, Na, K) are located in M4 site.	[23]
Ca <sub>8.82-z</sub> Ga(PO <sub>4</sub> ) <sub>7</sub> :0.18Ce <sup>3+</sup> , zMn <sup>2+</sup>	Ce <sup>3+</sup> /Mn <sup>2+</sup>	Two broad emission bands: 350–450 nm/380 nm (Ce <sup>3+</sup> emission) 600–700 nm/625 nm (Mn <sup>2+</sup> emission)	The concentration quenching was observed above 9 mol. % Mn <sup>2+</sup> ; the decreasing of quantum yield from 62.3% to 67 % with increasing Mn <sup>2+</sup> concentration was explained by energy loss during Ce <sup>3+</sup> → Mn <sup>2+</sup> energy transfer process.	[24]
Ca <sub>10</sub> K(PO <sub>4</sub> ) <sub>7</sub> :Eu <sup>2+</sup> , Mn <sup>2+</sup>	Eu <sup>2+</sup> /Mn <sup>2+</sup>	Two broad emission bands (λ <sub>ex</sub> = 347 nm): 425–500 nm/467 nm (Eu <sup>2+</sup> emission) 600–700 nm/634 nm (Mn <sup>2+</sup> emission)	Decreasing of PL intensity with increasing of Mn <sup>2+</sup> concentration. The concentration quenching was observed above 7 mol. % Mn <sup>2+</sup> ; resonant type of Eu <sup>2+</sup> → Mn <sup>2+</sup> energy transfer process via a dipole–quadrupole mechanism.	[14]
Ca <sub>9</sub> MgK(PO <sub>4</sub> ) <sub>7</sub> :Eu <sup>2+</sup> , Mn <sup>2+</sup>	Eu <sup>2+</sup> /Mn <sup>2+</sup>	Two broad emission bands (λ <sub>ex</sub> = 347 nm) 425–500 nm/467 nm (Eu <sup>2+</sup> emission) 600–700 nm/634 nm (Mn <sup>2+</sup> emission)	Resonant type of Eu <sup>2+</sup> → Mn <sup>2+</sup> energy transfer with mechanism via a dipole–quadrupole interaction.	[25]
Ca <sub>8</sub> ZnCe(PO <sub>4</sub> ) <sub>7</sub> :Eu <sup>2+</sup> , Mn <sup>2+</sup>	Ce <sup>3+</sup> /Eu <sup>2+</sup> /Mn <sup>2+</sup>	Three broad bands peaked (λ <sub>ex</sub> = 285 nm) 320–420 nm/375 nm (Ce <sup>3+</sup> emission) 450–575 nm/500 nm (Eu <sup>2+</sup> emission) 580–700 nm/645 nm (Mn <sup>2+</sup> emission)	The energy transfers of Ce <sup>3+</sup> → Eu <sup>2+</sup> /Mn <sup>2+</sup> and Eu <sup>2+</sup> → Mn <sup>2+</sup> ions were investigated. The emitting color can be adjusted from violet-blue to green/red-orange/white by doping/co-doping.	[26]

## 2. Materials and Methods

The series of phosphates Ca<sub>9-x</sub>Mn<sub>x</sub>Eu(PO<sub>4</sub>)<sub>7</sub> was synthesized by high-temperature solid-state route from simple oxides MnO<sub>2</sub> (99.9%), Eu<sub>2</sub>O<sub>3</sub> (99.9%), calcium hydrogen phosphate CaHPO<sub>4</sub>·2H<sub>2</sub>O (99.9%) and calcium carbonate CaCO<sub>3</sub> (99.9%). The reagents of standard grade were checked for purity and used without further purification. The raw materials were weighted and thoroughly grounded. The syntheses were carried out in air in alundum crucibles at 1100 °C for 50 h. Phase analysis using JCPDS PDF-4 database (ICDD, Newtown Square, PA, USA) revealed that the synthesized samples did not contain any reflections of the initial or impurity phases.

The chemical composition of Ca<sub>8</sub>MnEu(PO<sub>4</sub>)<sub>7</sub> was determined by energy-dispersive X-ray spectrometry (EDX) using scanning electron microscope (SEM) Tescan VEGA3 (Oxford Instruments, Abingdon, UK) equipped with an Oxford Instruments X-Max 50 silicon drift. The EDX analysis results were based on the Ca<sub>K</sub>, Mn<sub>K</sub>, Eu<sub>L</sub> and P<sub>K</sub> edge lines. The oxygen content was not quantified by EDX.

Powder X-ray diffraction (PXRD) patterns were obtained using Thermo ARL X'TRA (Bragg–Brentano geometry, Scintillator detector, CuKα radiation, λ = 1.5418 Å, Thermo Fisher Scientific, Waltham MA, USA). PXRD data were collected in 2θ range from 5° to 75° with 0.02° step at room temperature.

Synchrotron PXRD data for  $\text{Ca}_8\text{MnEu}(\text{PO}_4)_7$  were measured with a large Debye-Scherrer camera (home-made, NIMS, Tsukuba, Japan) at the BL15XU beamline of SPring-8. The intensity data were collected in  $2\theta$  range from  $1^\circ$  to  $60^\circ$  with step  $0.003^\circ$ . The incident beam was monochromatized at  $\lambda = 0.65298 \text{ \AA}$ . The samples were packed into Lindemann glass capillaries with an inner diameter of 0.1 mm, which were rotated during the measurement. The absorption coefficients were also measured. Rietveld analysis [27] was performed using JANA2006 software (by Petricek, V., Dusek, M. & Palatinus, L. Institute of Physics, Academy of Science of the Czech Republic, Praha) [28].

The second harmonic generation (SHG) signal was measured with a Q-switched YAG:Nd laser (home-made, Moscow, Russia) at  $\lambda_{\omega} = 1064 \text{ nm}$  in the reflection mode. The powder of  $\alpha\text{-SiO}_2$  (3–5  $\mu\text{m}$  particles size) was used as a standard to calibrate the intensity of the SHG signal ( $I_{2\omega}$ ). The final SHG value is a relation:  $I_{2\omega}(\text{sample})/I_{2\omega}(\text{SiO}_2)$ .

Differential scanning calorimetry (DSC) measurements were performed on an NETZSCH DSC 204 F1 calorimeter (NETZSCH, Selb, Germany) in the temperature range from 323 to 973 K with heating rate  $10 \text{ K}\cdot\text{min}^{-1}$  in nitrogen flow of  $40 \text{ mL}\cdot\text{min}^{-1}$ .

The electrical conductivity, dielectric permittivity  $\epsilon$  and dielectric loss tangent  $\text{tg } \delta$  in air were measured by the double-contact method in the frequency range of 1–106 Hz at 300–1270 K (heating rate of  $5 \text{ K}\cdot\text{min}^{-1}$ ), with the help of precision voltmeter Solartron 7081 (Schlumberger, Houston, TX, USA) and frequency response analyzer Solartron 1260 (Schlumberger, Houston, TX, USA). Ceramic pellet from  $\text{Ca}_8\text{MnEu}(\text{PO}_4)_7$  (1.5 mm thick and 5–6 mm in diameter) was prepared by pressing and sintering at 1473 K for 12 h. Pt paste was put on the flat surfaces of the pellet, and then it was heated at 1023 K for 4 h to produce platinum electrodes.

Magnetic measurements were performed on a SQUID magnetometer (Quantum Design, MPMS-XL-7T, Quantum Design, San Diego, CA, USA) from 400 K to 2 K at an applied field of 10 kOe. Isothermal magnetization measurements,  $M$  vs.  $H$ , were performed from 70 kOe to 0 Oe at  $T = 2 \text{ K}$ .

The surface chemical analysis of  $\text{Ca}_{9-x}\text{Mn}_x\text{Eu}(\text{PO}_4)_7$   $x = 0.2$  and  $x = 1.0$  phosphates was performed by XPS using a Axis Ultra DLD (Kratos Analytical, Manchester, UK) spectrometer with monochromatic  $\text{AlK}_{\alpha}$  source X-rays (1486.6 eV). The measurements were performed at pressure better than  $5 \times 10^{-7} \text{ Pa}$ . The area of the surface analyzed was  $\sim 300 \times 700 \mu\text{m}^2$ , which provided statistically reliable average results that represented the general surface of the compact powder. The resolution of the spectrometer measured as the full width at half maximum (FWHM) of the  $\text{Au}4f_{7/2}$  line was about 0.7 eV. The experiments were performed with charge neutralization and use of the C1s level (285.0 eV) arising from the saturated hydrocarbon contamination on the sample surface as the binding energy ( $E_b$ , eV) scale reference. Selected region spectra were recorded covering the Ca2s, Ca2p, P2s, P2p, Eu3d, Eu4p, Eu4d, Mn2p, O1s and C1s photoemission peaks. The XPS spectra were measured with an energy step size of 1 eV and a pass energy of 160 eV. The high-resolution XPS spectra were performed with an energy step size of 0.1 eV and a pass energy of 40 eV.

Luminescence excitation spectra and emission spectra under excitation in the UV region were measured using a 150 W xenon lamp (Oriel Instruments, Stratford, CT, USA) as an excitation source, an MDR-206 primary monochromator (Lomo, Saint-Petersburg, Russia) and a LOT-Oriel MS-257 spectrograph (Oriel Instruments, Stratford, CT, USA) equipped with a Marconi CCD detector (Marconi Applied Technologies Limited, Chelmsford, UK). Samples were mounted into a Cryotrade LN-120 vacuum optical cryostat (Cryotrade engineering, Moscow, Russia).

### 3. Results

#### 3.1. SEM Observations

The SEM image of  $\text{Ca}_8\text{MnEu}(\text{PO}_4)_7$  is shown in Figure 1. The sample consists of small particles from 2–5  $\mu\text{m}$  which are slightly agglomerate with each other. According to the EDX data, the ratio between Ca: Mn: Eu: P in  $\text{Ca}_8\text{MnEu}(\text{PO}_4)_7$  was determined as  $7.98 \pm 0.62$ :  $1.01 \pm 0.08$ :  $0.99 \pm 0.05$ :  $7.01 \pm 0.85$ . This ratio, defined by EDX data, is close to the expected composition.

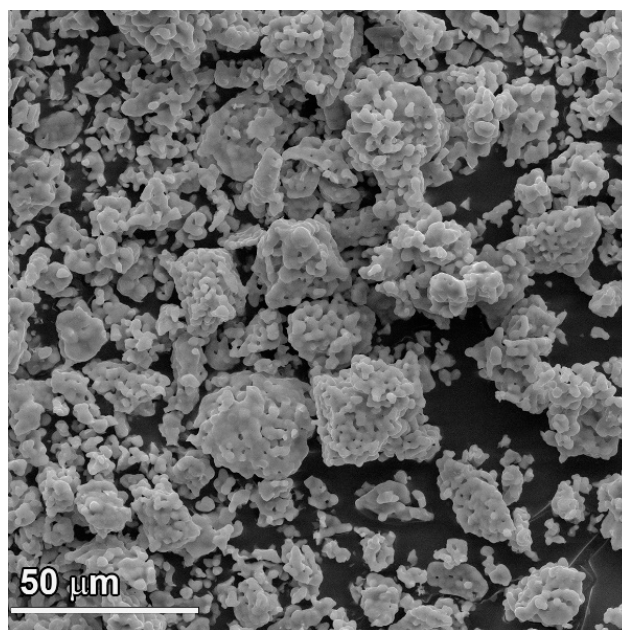


Figure 1. SEM image of  $\text{Ca}_8\text{MnEu}(\text{PO}_4)_7$ .

#### 3.2. SHG, DSC and Dielectric Spectroscopy Measurements

The SHG signal of  $\text{Ca}_8\text{MnEu}(\text{PO}_4)_7$  shows a very weak response. The value of the SHG signal ( $I_{2\omega}$ ) relative to the quartz standard  $I_{2\omega}(\text{SiO}_2)$  was  $I_{2\omega}/I_{2\omega}(\text{SiO}_2) < 0.1$ , which corresponds to the sensitivity limit of the device. Such a small SHG signal value is attributed to a centrosymmetric structure. Previously studied  $\text{Ca}_8\text{M}^{2+}\text{Eu}(\text{PO}_4)_7$  phosphates with  $\text{M}^{2+} = \text{Zn}^{2+}$  [29],  $\text{Mg}^{2+}$  [30],  $\text{Cd}^{2+}$  [31] showed similar small SHG values, and their structures were defined as centrosymmetric with the space group  $R\bar{3}c$ . The studied  $\text{Ca}_8\text{MnEu}(\text{PO}_4)_7$  phosphate complements the group of centrosymmetric  $\beta$ -TCP-type compounds.

For the series of phosphates  $\text{Ca}_{9-x}\text{Mn}_x\text{Eu}(\text{PO}_4)_7$ , the SHG signal shows a trend to decrease from 0.4 for  $\text{Ca}_9\text{Eu}(\text{PO}_4)_7$  ( $x = 0$ ) to 0 for  $\text{Ca}_8\text{MnEu}(\text{PO}_4)_7$  ( $x = 1$ ). This trend was observed in other  $\beta$ -TCP solid solutions,  $\text{Ca}_{9-x}\text{Mg}_x\text{RE}(\text{PO}_4)_7$ ,  $\text{RE} = \text{Dy}^{3+}$  [32],  $\text{Eu}^{3+}$  [33] and  $\text{Ca}_{9-x}\text{Zn}_x\text{RE}(\text{PO}_4)_7$  with  $\text{RE} = \text{Tb}^{3+}$  [34],  $\text{Ho}^{3+}$  [35],  $\text{Eu}^{3+}$  [29],  $\text{La}^{3+}$  [36] according to symmetry inhomogeneity of the  $\beta$ -TCP structure.

The fragments of DSC curves for  $\text{Ca}_8\text{MnEu}(\text{PO}_4)_7$  are showed in Figure 2. DSC curves in the heating and cooling cycles point to the presence of only one peak at 501 and 520  $^\circ\text{C}$ , respectively. These peaks are attributed to the first-order phase transition and have a reversible character.

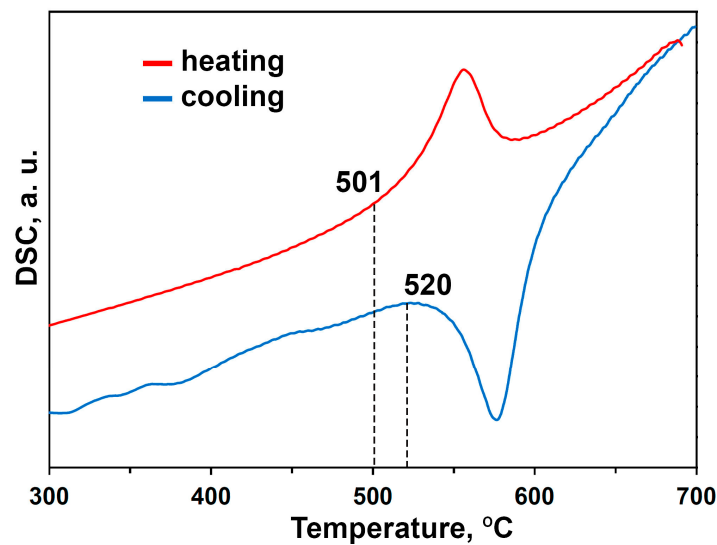


**Figure 2.** DSC curves in the heating/cooling cycles for Ca<sub>8</sub>MnEu(PO<sub>4</sub>)<sub>7</sub>. The heating/cooling rate is 10 K/min.

The temperature dependencies of the dielectric permittivity  $\epsilon(T)$  and the dielectric loss tangent  $\text{tg} \delta(T)$  at different frequencies for Ca<sub>8</sub>MnEu(PO<sub>4</sub>)<sub>7</sub> are shown in Figures 3a and 3b, respectively.  $\epsilon(T)$  increases with heating and reaches the phase transition at 525–575 °C with maximum at 550 °C (Figure 3a). A monotonous increase of  $\epsilon(T)$  to around Curie temperature ( $T_c$ ) seems to be the characteristic behavior. The location of the maximum on the curves does not depend on the frequency (Figure 3a). Such a maximum can characterize both ferroelectric and antiferroelectric phase transitions. However, the absence of an anomaly in  $\text{tg} \delta(T)$  curve at a temperature of 500–1200 °C (Figure 3b) indicates the antiferroelectric character of the phase transition [37,38].

The absence of the SHG signal and the presence of an antiferroelectric phase transition on  $\epsilon(T)$  along with effects on DSC curves confirm the centrosymmetric structure of Ca<sub>8</sub>MnEu(PO<sub>4</sub>)<sub>7</sub>. Since the polar and nonpolar space groups  $R3c$  and  $R\bar{3}c$  in the  $\beta$ -TCP-type compounds are practically indistinguishable from PXRD data [33], previously it was proved by electron diffraction that Ca<sub>8</sub>MgEu(PO<sub>4</sub>)<sub>7</sub> [37] crystallizes in the centrosymmetric group  $R\bar{3}c$ , and during the phase transition, the symmetry changes from  $R\bar{3}c$  to  $R\bar{3}m$  [37].

The temperature position of the phase transition in Ca<sub>8</sub>MnEu(PO<sub>4</sub>)<sub>7</sub> exceeds these values for Ca<sub>8</sub>ZnEu(PO<sub>4</sub>)<sub>7</sub> ( $T_c \sim 547$  °C) [29] and Ca<sub>8</sub>MgEu(PO<sub>4</sub>)<sub>7</sub> ( $T_c \sim 507$  °C) [33]. This fact is due to the difference in the values of the ionic radii of  $M^{2+}$  in Ca<sub>8</sub>MEu(PO<sub>4</sub>)<sub>7</sub>. The phase transition occurs at lower temperatures when the smaller ion is placed in the M5 site. Since Mn<sup>2+</sup> is the largest among these ions (Zn<sup>2+</sup>, Mg<sup>2+</sup>, Mn<sup>2+</sup>),  $T_c$  shows the biggest value. However, the replacement Ca<sup>2+</sup> → Mn<sup>2+</sup> does not significantly affect the phase transition temperature, which is 573 °C for Ca<sub>9</sub>Eu(PO<sub>4</sub>)<sub>7</sub> [35].

The temperature dependence of the electric conductivity ( $\sigma$ ) of Ca<sub>8</sub>MnEu(PO<sub>4</sub>)<sub>7</sub> at 50 kHz is shown in Figure 4 in the Arrhenius coordinates  $\log(\sigma) - (10^3/T)$ . The electroconductivity of Ca<sub>8</sub>MnEu(PO<sub>4</sub>)<sub>7</sub> is rising with the temperature increasing. The abrupt change in  $\sigma$  at 820–860 K is due to the rearrangement at the antiferroelectric/paraelectric phase transition ( $R\bar{3}c \leftrightarrow R\bar{3}m$ ). Since the conduction temperature during heating is higher than during cooling, such a change in  $\sigma$  also indicates a first-order phase transition. The temperature behavior of the electroconductivity in Ca<sub>8</sub>MnEu(PO<sub>4</sub>)<sub>7</sub> is similar to other phosphates with the common formula Ca<sub>8</sub>M<sup>2+</sup>RE<sup>3+</sup>(PO<sub>4</sub>)<sub>7</sub> [30,31,39] and is a consequence of the mobility of Ca<sup>2+</sup> ions [40].

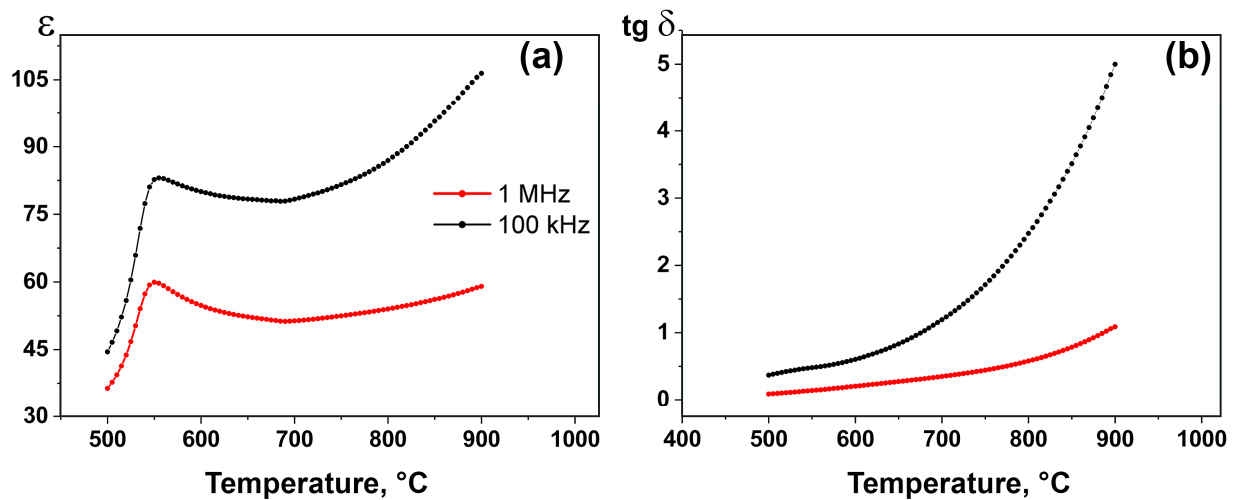


**Figure 3.** The temperature dependence of the dielectric permittivity  $\epsilon(T)$  (a) and the dielectric loss tangent ( $\text{tg } \delta$ ) (b) for  $\text{Ca}_8\text{MnEu}(\text{PO}_4)_7$  at 50 kHz and 1 MHz (on heating).

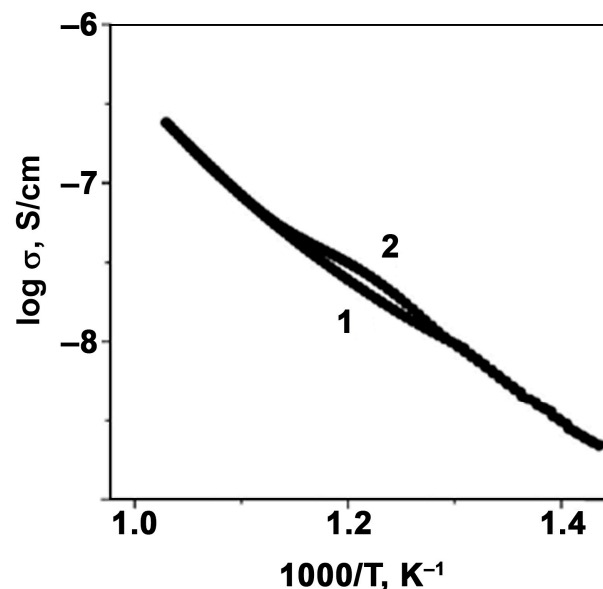


**Figure 4.** Electric conductivity of  $\text{Ca}_8\text{MnEu}(\text{PO}_4)_7$  at 50 kHz on heating (1) and cooling (2).

### 3.3. PXRD Study

PXRD pattern of  $\text{Ca}_8\text{MnEu}(\text{PO}_4)_7$  is similar to other compounds with the  $\beta$ -TCP-type structure (Figure 5). The absence of any impurity reflections on the PXRD pattern shows that  $\text{Eu}^{3+}$  and  $\text{Mn}^{2+}$  ions were completely involved in the structure.  $\beta$ - $\text{Ca}_3(\text{PO}_4)_2$  structure (sp.gr.  $R3c$ ,  $Z = 6$ ) is a rather rigid structure and consists of isolated tetrahedra  $\text{PO}_4$  that connect  $\text{CaO}_n$  polyhedra into a 3D frame by common vertices [41]. The  $\text{Ca}^{2+}$  ions are located in sites M1–M5, where M1–M3 and M5 sites are fully occupied, while M4 sites are partly filled and M6 sites are fully vacant.

No vacancies in the anionic sublattice can appear in the  $\beta$ - $\text{Ca}_3(\text{PO}_4)_2$ -type structure, even during heterovalent substitutions, when  $[\text{PO}_4]^{3-}$  is replaced by  $[\text{GeO}_4]^{4-}$  [42] or  $[\text{SO}_4]^{2-}$  [43], for instance. Formation of phase-pure phases in these cases requires charge compensation. So, phosphorus atoms fully occupy three (P1, P2 and P3) tetrahedra sites. The symmetry changing  $R3c \rightarrow R\bar{3}c$  results in an equivalence of M1 and M2 sites in the cationic sublattice and  $\text{P2O}_4$  and  $\text{P3O}_4$  tetrahedra in the anionic sublattice. M5, M3 and P1

sites are located in the center of symmetry, and P1 is in the half-occupied special position 12c. Atoms O1 and O2 are located in half-occupied positions 12c and 36f, respectively.

The atomic coordinates for  $\text{Ca}_8\text{MgEu}(\text{PO}_4)_7$  were used as a starting model for synchrotron data refinement for  $\text{Ca}_8\text{MnEu}(\text{PO}_4)_7$ . Manganese ions were refined in the octahedral M5 site, while Eu ions were distributed through M1 and M3 sites with the preference occupation in the M1 site (Table S1 of the Supporting Information). After the structure refinement in an  $R\bar{3}c$  model, a good agreement between the calculated and the experimental synchrotron PXRD patterns was observed, as it can be seen from the Figure 5 difference plot. Figure 5 shows fragments of the observed, calculated and difference synchrotron PXRD patterns of  $\text{Ca}_8\text{MnEu}(\text{PO}_4)_7$ . Other numerical characteristics showing the quality of the structure refinements are given in Table 2. The fractional atomic coordinates, isotropic atomic displacement parameters and cation occupancies are listed in Table S1 of the Supporting Information. The main interatomic distances are listed in Table S2 of the Supporting Information. CCDC 2237297 contains the supplementary crystallographic data for this paper.

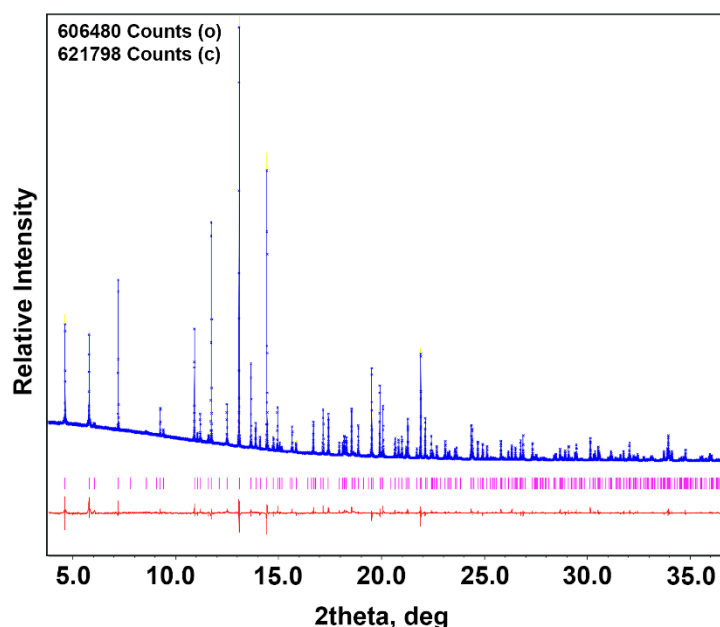


**Figure 5.** Observed (blue crosses), calculated (blue line) and difference (red line from below) synchrotron PXRD patterns for  $\text{Ca}_8\text{MnEu}(\text{PO}_4)_7$ . Magenta bars denote the peak positions of possible Bragg reflections.

**Table 2.** Crystallographic data for  $\text{Ca}_8\text{MnEu}(\text{PO}_4)_7$  (SG  $R\bar{3}c$ ,  $Z = 6$ ,  $T = 293$  K).

Sample Composition	$\text{Ca}_8\text{MnEu}(\text{PO}_4)_7$
Lattice parameters: $a$ , Å	10.39826(1)
$c$ , Å	37.17350(5)
Unit cell volume $V$ , Å <sup>3</sup>	3480.851(7)
Calculated density, g/cm <sup>3</sup>	3.413
Data Collection:	
Diffractometer	BL15XU beamline of SPring-8
Radiation/Wavelength ( $\lambda$ , Å)	Synchrotron/0.65298
Absorption coefficient, $\mu$ (mm <sup>-1</sup> )	4.381
F(000)	3462

Table 2. Cont.

Sample Composition	Ca <sub>8</sub> MnEu(PO <sub>4</sub> ) <sub>7</sub>
2θ range (°)	2.040–60.237
Step scan (2θ)	0.003
I <sub>max</sub>	606,480
Number of points	19,391
Refinement:	
Refinement	Rietveld
Background function	Legendre polynoms, 15 terms
No. of reflections (all/observed)	945/922
No. of refined parameters/refined atomic parameters	43/34
R and R <sub>w</sub> (%) for Bragg reflections (R <sub>all</sub> /R <sub>obs</sub> )	5.29/5.95 and 5.05/4.81
R <sub>p</sub> and R <sub>wp</sub> ; R <sub>exp</sub>	2.06, 3.31, 0.63
Goodness of fit (ChiQ)	5.25
Max./min. residual density(e) (Å <sup>3</sup> )	0.65/−0.88

Figure 6a shows PXRD patterns of Ca<sub>9−x</sub>Mn<sub>x</sub>Eu(PO<sub>4</sub>)<sub>7</sub> solid solutions. All the diffraction peaks are matched with β-TCP (PDF#4 Card No. 00-09-0169). Moreover, a shifting of the reflections with the increasing of manganese concentration can be observed (Figure 6b). The reflections move toward larger angles according to Bragg's rule and difference between the ionic radii of Ca<sup>2+</sup> (*r*<sub>IV</sub> = 1.00 Å) and Mn<sup>2+</sup> (*r*<sub>IV</sub> = 0.83 Å). The absence of the impurity phases in PXRD patterns and reflections shifting show the successful incorporation of Mn<sup>2+</sup> ions in the β-TCP structure in all samples.

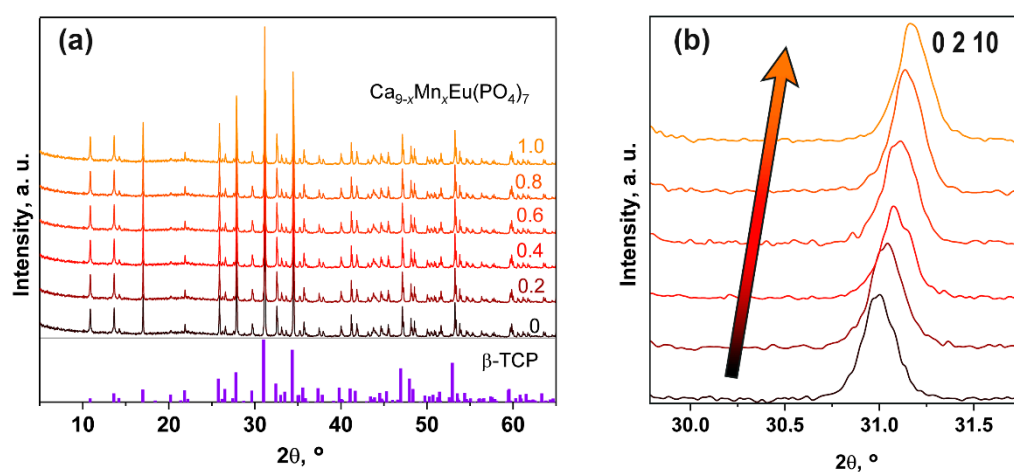


**Figure 6.** PXRD patterns of Ca<sub>9−x</sub>Mn<sub>x</sub>Eu(PO<sub>4</sub>)<sub>7</sub> and the positions of Bragg reflections of β-TCP (β-Ca<sub>3</sub>(PO<sub>4</sub>)<sub>2</sub>, PDF#4 Card No. 00-09-0169) (a); The enlarged main reflection (0 2 10) of Ca<sub>9−x</sub>Mn<sub>x</sub>Eu(PO<sub>4</sub>)<sub>7</sub> solid solution (b).

### 3.4. Magnetic Measurements

The inverse magnetic susceptibilities follow the Curie–Weiss law. Between 200 and 395 K, the inverse magnetic susceptibilities are fit by the Curie–Weiss equation:

$$\chi(T) = \mu_{\text{eff}}^2 N (3k_{\text{B}}(T - \theta))^{-1},$$

where  $\mu_{\text{eff}}$  is an effective magnetic moment,  $N$  is Avogadro's number,  $k_{\text{B}}$  is Boltzmann's constant and  $\theta$  is the Curie–Weiss temperature. The fitting parameters for Ca<sub>8</sub>MnEu(PO<sub>4</sub>)<sub>7</sub> were  $\mu_{\text{eff}} = 7.076(2)$  ( $\mu_{\text{B}}$ /f.u.),  $\mu_{\text{calc}} = 6.823$  ( $\mu_{\text{B}}$ /f.u.) and  $\theta = -27.2(2)$  K. The  $\mu_{\text{eff}}$  value was in good agreement with the theoretical value, where  $\mu_{\text{calc}}$  is calculated using  $3.4\mu_{\text{B}}$  for Eu<sup>3+</sup> [44] (Figure 7).

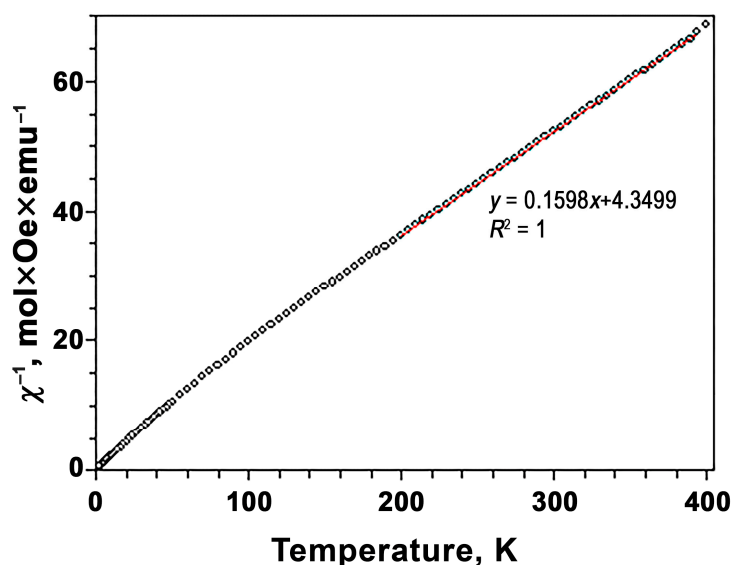


Figure 7. Temperature-dependent inverse magnetic susceptibility curve of  $\text{Ca}_8\text{MnEu}(\text{PO}_4)_7$  at  $H = 10$  kOe with fitting results (line).

The  $M$  vs.  $H$  curve of  $\text{Ca}_8\text{MnEu}(\text{PO}_4)_7$  followed very well the Brillouin function with  $g = 2$ ,  $S = 5/2$  and  $T = 2$  K, as expected for a free  $\text{Mn}^{2+}$  cation (Figure 8). The magnetization at 2 K and 70 kOe reached  $5.047$  ( $\mu_B/\text{f.u.}$ ).

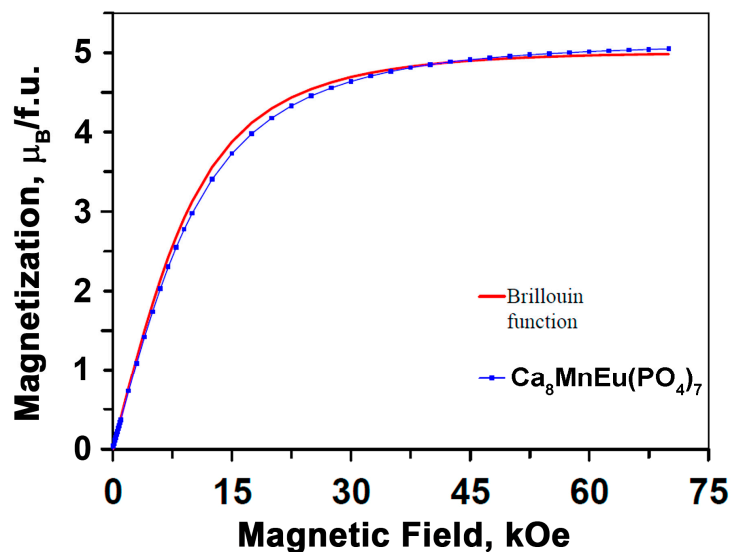
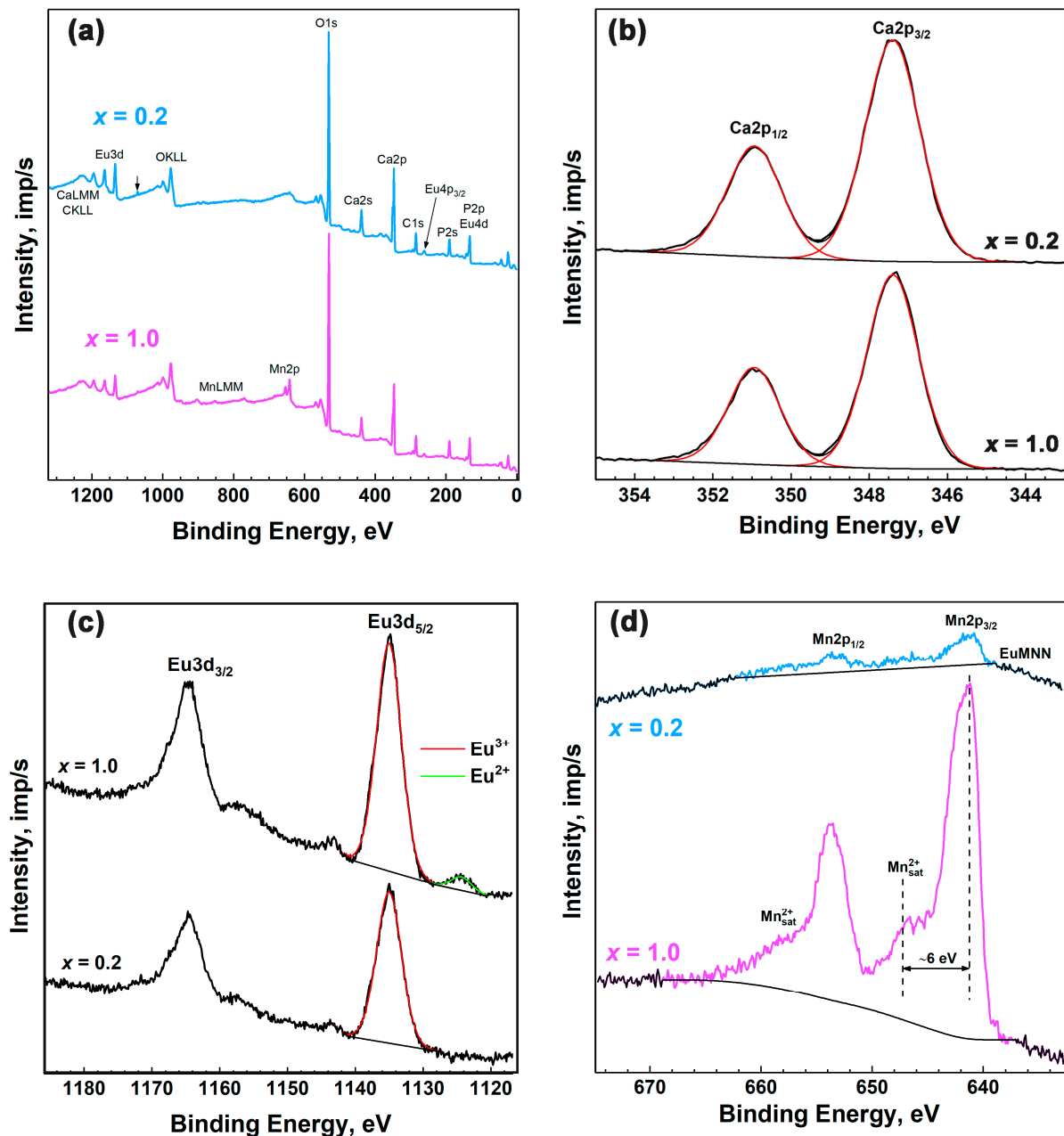


Figure 8.  $M$  versus  $H$  curves at  $T = 2$  K for  $\text{Ca}_8\text{MnEu}(\text{PO}_4)_7$ . The red line shows the Brillouin function with  $g = 2$ ,  $S = 5/2$  and  $T = 2$  K.

### 3.5. XPS Study

In the survey XPS scans of  $\text{Ca}_{9-x}\text{Mn}_x\text{Eu}(\text{PO}_4)_7$   $x = 0.2$  and  $x = 1.0$  samples (Figure 9a), the lines of calcium, europium, manganese, phosphorus, carbon and oxygen were observed.  $\text{Ca}2p$  XPS spectra (Figure 9b) were used for energy calibration of samples' spectra to eliminate the charging effect.



**Figure 9.** The XPS survey spectrum (a) and high-resolution XPS spectra of Ca2p (b), Eu3d (c) and Mn2p (d) peaks of  $\text{Ca}_{9-x}\text{Mn}_x\text{Eu}(\text{PO}_4)_7$  with  $x = 0.2$  and  $1.0$ .

In the Eu3d spectra of the samples (Figure 9c), the doublet of lines Eu3d<sub>5/2</sub> and Eu3d<sub>3/2</sub> was observed with 1135.0 and 1164.5 eV binding energies. These values are typical for the Eu<sup>3+</sup> ion [45]. The additional Eu3d<sub>5/2</sub> component with 1124.4 eV binding energy can be distinguished in the  $\text{Ca}_8\text{MnEu}(\text{PO}_4)_7$  spectrum. This component is attributed to Eu<sup>2+</sup> [46–49]. The quantity of divalent europium in  $\text{Ca}_8\text{MnEu}(\text{PO}_4)_7$  is about 5% of the total europium content. At the same time, in [45,50,51], the appearance of such low-energy components is associated with shake-down satellites from the main lines of trivalent europium and indicates that the intensity of such satellites can vary depending on the specific compound of trivalent europium.

The Mn2p XPS shape of the  $\text{Ca}_8\text{MnEu}(\text{PO}_4)_7$  (Figure 9d) is typical of the divalent state of manganese [52]. The spectrum exhibits pronounced shake-up satellites characteristic of divalent manganese, which are shifted from the main peaks by approximately 6 eV towards

higher binding energies. Similarly, in the Mn3s spectrum of  $\text{Ca}_8\text{MnEu}(\text{PO}_4)_7$  (Figure 10), the splitting typical for divalent manganese is observed (Table 2). The Mn2p and Mn3s spectra of  $\text{Ca}_{8.8}\text{Mn}_{0.2}\text{Eu}(\text{PO}_4)_7$  are close in shape to  $\text{Ca}_8\text{MnEu}(\text{PO}_4)_7$ . However, due to the significantly lower content of manganese in this sample, the spectra are observed to be noticeably noisier. The comparison of the parameters Mn2p and Mn3s spectra with reference data are listed in Table 3.

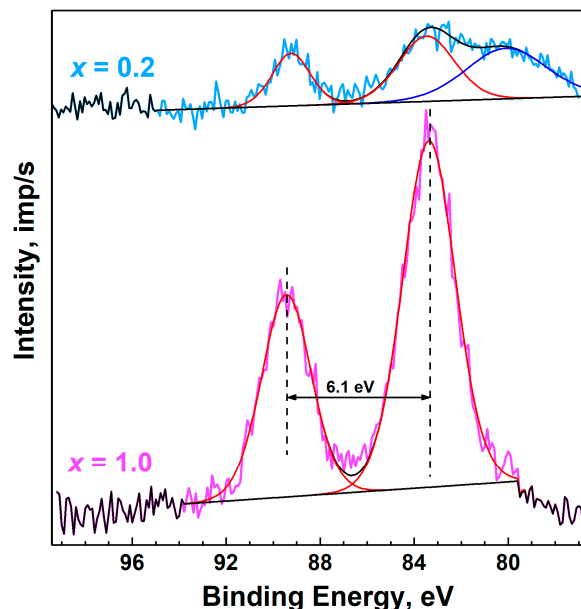


Figure 10. High-resolution XPS spectra of Mn3s peaks of  $\text{Ca}_{9-x}\text{Mn}_x\text{Eu}(\text{PO}_4)_7$   $x = 0.2$  and  $1.0$ .

Table 3. Relative position of the satellite ( $\Delta\text{Mn2p}_{\text{sat}}$ ) in Mn2p XPS spectra and splitting ( $\Delta\text{Mn3s}$ ) Mn3s XPS spectra of the studied  $\text{Ca}_{9-x}\text{Mn}_x\text{Eu}(\text{PO}_4)_7$  ( $x = 0.2$  and  $1.0$ ) samples and reference manganese oxides, eV.

Sample	$\Delta\text{Mn2p}_{\text{sat}}$	$\Delta\text{Mn3s}$	Reference
$\text{Ca}_8\text{MnEu}(\text{PO}_4)_7$	~6.0	6.1	This work
$\text{Ca}_{8.8}\text{Mn}_{0.2}\text{Eu}(\text{PO}_4)_7$	~6.0	5.8	This work
MnO	~6.0	6.1	[53,54]
$\text{Mn}_2\text{O}_3$	10.1	5.4	[55]
$\text{MnO}_2$	11.8	4.4	[56]

### 3.6. Photoluminescent Properties

Normalized photoluminescence excitation (PLE) spectra for one of the samples are shown in Figure 11. PLE spectra monitored at 440 nm exhibit an unresolved broad band from 300 to 400 nm, peaking at 365 nm, which originated from the  $\text{Eu}^{2+}$  4f-5d-allowed transition (Figure 9). At 620 nm, the PLE spectrum consists of sharp lines attributed to transitions of  $\text{Eu}^{3+}$  from the ground  ${}^7\text{F}_0$  level to excited levels. The bands are located at 318 nm ( ${}^7\text{F}_0 \rightarrow {}^5\text{H}_3$ ), 362 nm ( ${}^7\text{F}_0 \rightarrow {}^5\text{D}_4$ ), 378 nm ( ${}^7\text{F}_0 \rightarrow {}^5\text{G}_1$ ), 382 nm ( ${}^7\text{F}_0 \rightarrow {}^5\text{L}_7$ ), 395 nm ( ${}^7\text{F}_0 \rightarrow {}^5\text{L}_6$ ), 416 nm ( ${}^7\text{F}_0 \rightarrow {}^5\text{D}_3$ ) and 465 nm ( ${}^7\text{F}_0 \rightarrow {}^5\text{D}_4$ ), and the area at 250–300 nm is attributed to the charge transfer band (Figure 9). The other samples from the series show the same spectra, and the main difference is in the intensity of the spectra.

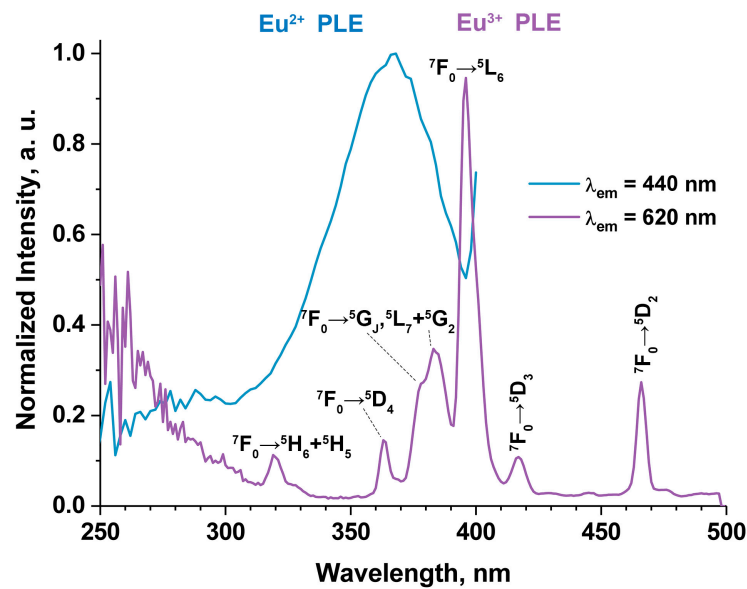


Figure 11. Normalized PLE spectra of  $\text{Ca}_{8.2}\text{Mn}_{0.8}\text{Eu}(\text{PO}_4)_7$  at  $\lambda_{\text{em}} = 440$  and  $620$  nm.

Figure 12 shows PL spectra of  $\text{Ca}_{8.2}\text{Mn}_{0.8}\text{Eu}(\text{PO}_4)_7$  at different excitation wavelengths. The broad unresolved emission band from  $400$  to  $700$  nm appearing under  $370$  nm excitation can be attributed to the  $4f^65d^1 \rightarrow 4f^7$  transition of  $\text{Eu}^{2+}$  [57]. The band is asymmetrical and peaked at  $440$  nm. It arises from different crystallographic sites occupied by Eu atoms in the  $\text{Ca}_{8.2}\text{Mn}_{0.8}\text{Eu}(\text{PO}_4)_7$  structure. Since the space group in this sample is  $R3c$ , there are M1–M3 sites occupied by Eu atoms, and several components in the  $\text{Eu}^{2+}$  emission can be distinguished [21]. The emission bands from  $\text{Eu}^{3+}$  are also observed under  $\lambda_{\text{ex}} = 370$  nm; however, their intensity is very low (Figure 12). The location of these lines can be determined at  $591$  nm ( $^5\text{D}_0 \rightarrow ^7\text{F}_1$ ),  $615$  nm ( $^5\text{D}_0 \rightarrow ^7\text{F}_2$ ),  $652$  nm ( $^5\text{D}_0 \rightarrow ^7\text{F}_3$ ) and  $698$  nm ( $^5\text{D}_0 \rightarrow ^7\text{F}_4$ ).

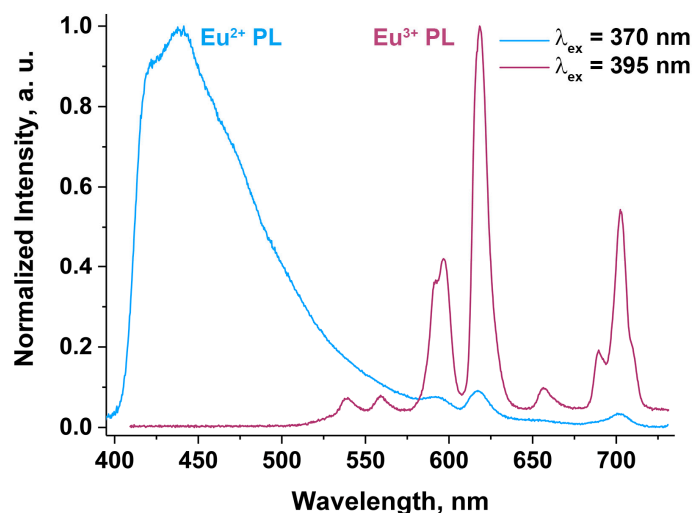
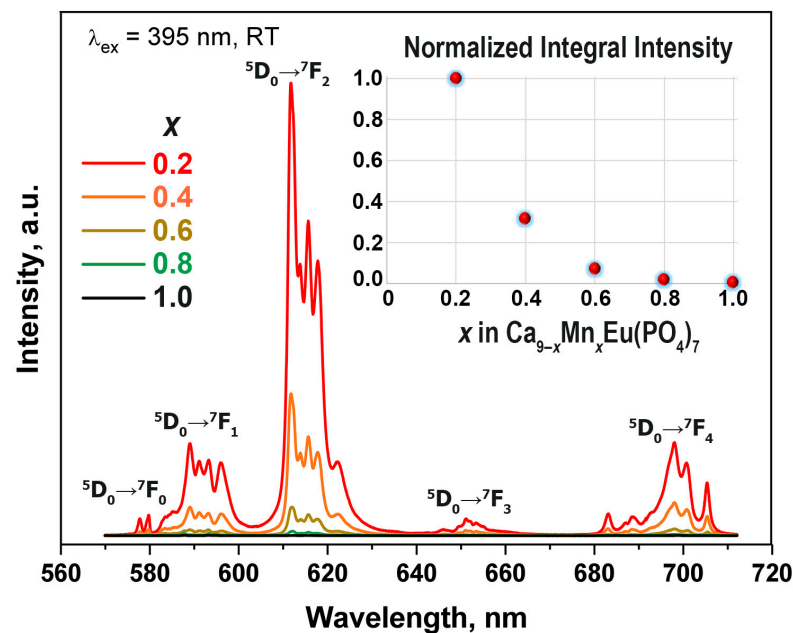


Figure 12. Normalized PL spectra of  $\text{Ca}_{9-x}\text{Mn}_x\text{Eu}(\text{PO}_4)_7$  with  $x = 0.8$  at  $\lambda_{\text{ex}} = 370$  nm and  $395$  nm.

Under  $395$  nm, the excitation PL spectra consist of the typical bands of  $\text{Eu}^{3+}$  emission (Figure 12). The presence of two types of Eu emission is related to partial abnormal self-reduction in the  $\beta$ -TCP host in agreement with XPS data. The locations of these bands are  $593$  nm ( $^5\text{D}_0 \rightarrow ^7\text{F}_1$ ),  $618$  nm ( $^5\text{D}_0 \rightarrow ^7\text{F}_2$ ),  $655$  nm ( $^5\text{D}_0 \rightarrow ^7\text{F}_3$ ) and  $701$  nm ( $^5\text{D}_0 \rightarrow ^7\text{F}_4$ ). The insignificant shifting of the peaks from  $370$  nm excitation is attributed to poor resolution

of  $\text{Eu}^{3+}$  emission at  $\lambda_{\text{ex}} = 370$  nm. Moreover, the transitions from higher-level  $^5\text{D}_1$  to  $^7\text{F}_1$  (535 nm) and  $^7\text{F}_2$  (555 nm) and  $^7\text{F}_2$  (555 nm) in terms of ground state can be observed (Figure 12).

PL spectra for  $\text{Ca}_{9-x}\text{Mn}_x\text{Eu}(\text{PO}_4)_7$  solid solutions at 395 nm excitation with high resolution are shown in Figure 13. The spectra consist of transitions from  $^5\text{D}_0$  excited level to  $^7\text{F}_0$  (579 nm),  $^7\text{F}_1$  (589 nm),  $^7\text{F}_2$  (612 nm),  $^7\text{F}_3$  (652 nm) and  $^7\text{F}_4$  (697 nm) levels. The normalized integral intensity of luminescence can be observed from the inset in Figure 13. It can be seen that PL intensity dramatically decreases with  $\text{Mn}^{2+}$  doping. This trend contradicts with the other  $\text{Ca}_{9-x}\text{M}_x\text{Eu}(\text{PO}_4)_7$  ( $M = \text{Zn}^{2+}, \text{Mg}^{2+}$ ) [29] solid solutions, where changing of the symmetry from polar  $R3c$  to nonpolar  $R\bar{3}c$  leads to increasing of the luminescence intensity. However, such behavior of PL intensity in  $\text{Eu}^{3+}$  and  $\text{Mn}^{2+}$  co-doped isostructural  $\text{Ca}_3(\text{VO}_4)_2$  was observed in [58]. The quenching of  $\text{Eu}^{3+}$  emission by  $\text{Mn}^{2+}$  doping in the  $\beta$ -TCP host is caused by the energy transfer from  $\text{Eu}^{3+}$  to  $\text{Mn}^{2+}$ ; however, the effective emission from  $\text{Mn}^{2+}$  ions is absent (Figures 12 and 13). The energy transfer can be relaxed by the  $^4\text{T}_1$  energy level of  $\text{Mn}^{2+}$  and then nonradiative relaxation to the  $^6\text{A}_1$  ground state of  $\text{Mn}^{2+}$  ions. Moreover, the emission from  $\text{Mn}^{2+}$  can be overlapped with the  $^5\text{D}_0 \rightarrow ^7\text{F}_3$  transition of  $\text{Eu}^{3+}$ . In addition, the substitution  $\text{Ca}^{2+} \rightarrow \text{Mn}^{2+}$  is accompanied by the  $R3c \rightarrow R\bar{3}c$  symmetry changing and the formation of defects in the structure, which may act as quenching centers of photoluminescence.



**Figure 13.** PL spectra for  $\text{Ca}_{9-x}\text{Mn}_x\text{Eu}(\text{PO}_4)_7$  at  $\lambda_{\text{ex}} = 395$  nm; the inset shows the dependence of normalized integral intensity on the  $\text{Mn}^{2+}$  concentration in  $\text{Ca}_{9-x}\text{Mn}_x\text{Eu}(\text{PO}_4)_7$ .

PL spectra for  $\text{Ca}_{9-x}\text{Mn}_x\text{Eu}(\text{PO}_4)_7$  solid solutions at 370 nm excitation are shown in Figure 14a. The intensity of  $\text{Eu}^{3+}$  emission also decreases with rising of  $\text{Mn}^{2+}$  concentration. Simultaneously, the intensity of the band attributed to  $\text{Eu}^{2+}$  emission (at  $\sim 450$  nm) increases. Such behavior can be clearly observed from the dependence of normalized integral intensity of  $\text{Eu}^{2+}$  and  $\text{Eu}^{3+}$  emission on  $\text{Mn}^{2+}$  concentration (Figure 14b). The position and profile of the  $\text{Eu}^{2+}$  band do not change with the  $\text{Mn}^{2+}$  concentration, which points to the invariability of the surrounding crystal field strength. Actually, since Eu and Mn atoms occupy different crystal sites in the  $\beta$ -TCP structure, the environment of Eu does not change. The rising of the  $\text{Eu}^{2+}$  band intensity (Figure 14a) can be attributed to the increasing of its concentration in the samples. This conclusion also follows from the XPS data.

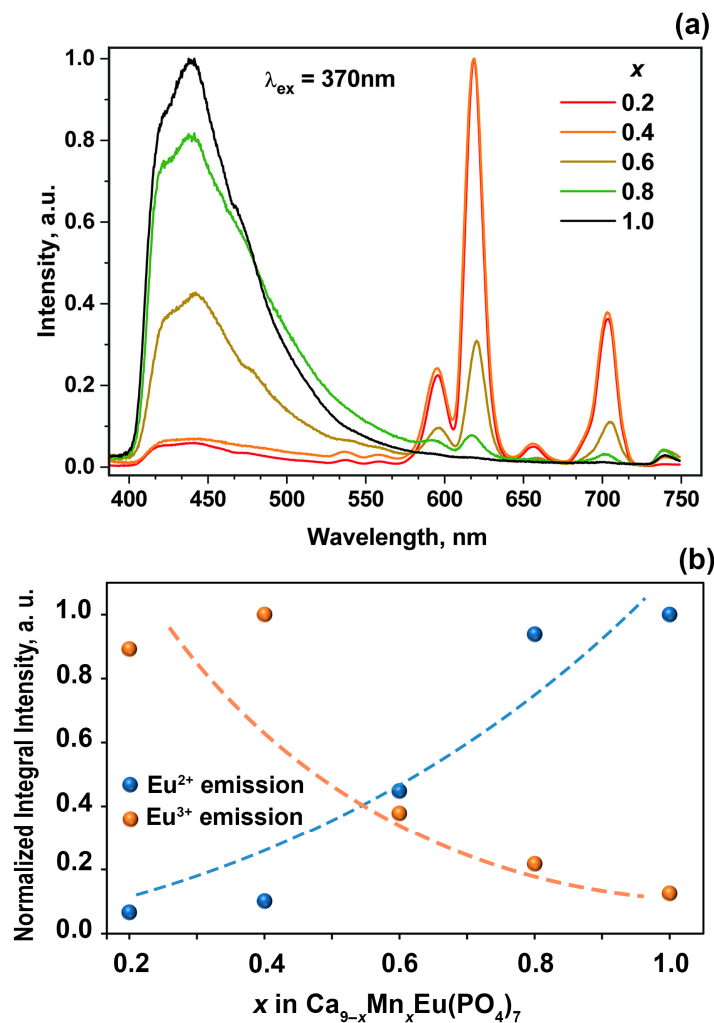


**Figure 14.** (a) PL spectra for  $\text{Ca}_{9-x}\text{Mn}_x\text{Eu}(\text{PO}_4)_7$  at  $\lambda_{\text{ex}} = 370 \text{ nm}$ ; (b) the dependence of normalized integral intensity of  $\text{Eu}^{2+}$  and  $\text{Eu}^{3+}$  emission ( $\lambda_{\text{ex}} = 370 \text{ nm}$ ).

To study the evolution of the  $\beta$ -TCP structure in  $\text{Ca}_{9-x}\text{Mn}_x\text{Eu}(\text{PO}_4)_7$  solid solutions, the hypersensitive  ${}^5\text{D}_0 \rightarrow {}^7\text{F}_0$  transition was analyzed. Figure 15 shows an enlarged part of luminescence spectra with the  ${}^5\text{D}_0 \rightarrow {}^7\text{F}_0$  transition. For the sample with the smallest  $\text{Mn}^{2+}$  concentration ( $x = 0.2$ ), the presence of nonsymmetrical well-separated bands can be observed (Figure 15a). These peaks reveal the nonequivalent environments of Eu atoms in the structure. The intensity of the  ${}^5\text{D}_0 \rightarrow {}^7\text{F}_0$  transition decreases with the rising of  $\text{Mn}^{2+}$  in  $\text{Ca}_{9-x}\text{Mn}_x\text{Eu}(\text{PO}_4)_7$  and becomes indistinguishable in samples with  $x = 0.8$  and 1.0. According to this, the analysis of the asymmetry ratio ( $R/O$ ) can provide the reliable information of the structure's evolution.  $R/O$  value can be calculated from the observed spectra using the formula [33]:

$$R/O = \frac{\int_{604 \text{ nm}}^{638 \text{ nm}} {}^5\text{D}_0 \rightarrow {}^7\text{F}_2}{\int_{518 \text{ nm}}^{604 \text{ nm}} {}^5\text{D}_0 \rightarrow {}^7\text{F}_1}$$

The dependence of  $R/O$  on  $\text{Mn}^{2+}$  concentration is shown in Figure 15b. The decreasing of  $R/O$  to  $\sim 1$  for  $\text{Ca}_8\text{MnEu}(\text{PO}_4)_7$  is attributed to the decreasing of the local distortion of the Eu environment in agreement with the structural data.

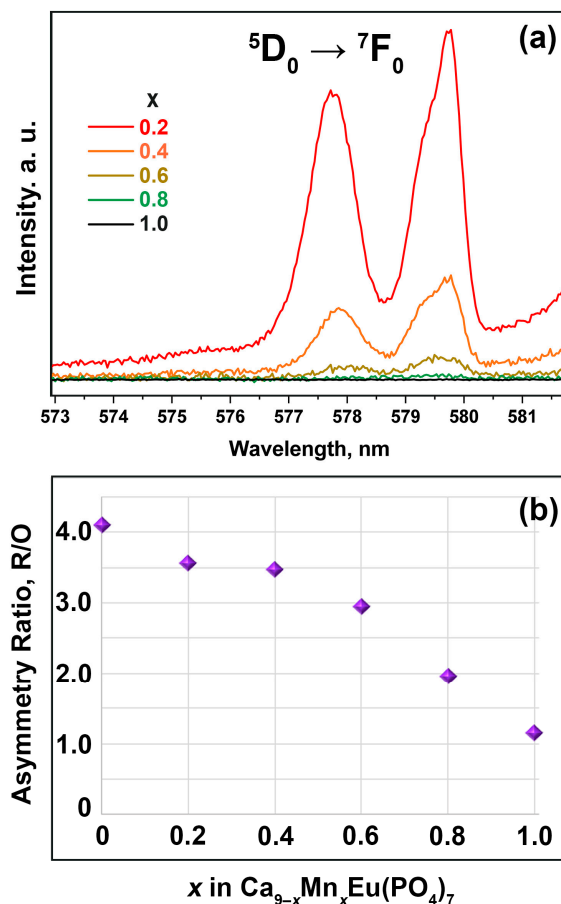


Figure 15. (a)  ${}^5D_0 \rightarrow {}^7F_0$  transition in  $\text{Ca}_{9-x}\text{Mn}_x\text{Eu}(\text{PO}_4)_7$  at  $\lambda_{\text{ex}} = 395$  nm; (b) the dependence of normalized integral intensity of  $\text{Eu}^{2+}$  and  $\text{Eu}^{3+}$  emission ( $\lambda_{\text{ex}} = 370$  nm).

#### 4. Discussion

The abnormal reduction  $\text{Eu}^{3+} \rightarrow \text{Eu}^{2+}$  in inorganic phosphors prepared using high-temperature solid-state reactions in air was observed in numerous studies [59–61]. Usually, this reduction leads to the coexistence of two types of europium oxidation states. There is no information on the full reduction of  $\text{Eu}^{3+}$  into  $\text{Eu}^{2+}$  in non-reduction media, so it is difficult to control the efficiency of reduction and luminescence intensity [62]. However, it should be noted that Mn ions in our study were fully reduced from  $\text{Mn}^{4+}$  ( $\text{MnO}_2$  as initial phase) to the  $\text{Mn}^{2+}$  state, which was shown by XPS and PL measurements.

The conditions for the abnormal reduction in oxosalts phosphors obtained in air using a high-temperature solid-state reaction were proposed in [63]. These conditions meet the requirements in the  $\beta$ -TCP type host:

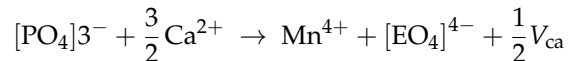
- (1) There are no oxidizing ions in the structure;
- (2) The  $\beta$ -TCP-type host is based on tetrahedral anion groups ( $\text{PO}_4^{3-}$ );
- (3) The doped ions ( $\text{Eu}^{3+}$  and  $\text{Mn}^{4+}$ ) substitute the sites with lower valences ( $\text{Ca}^{2+}$ ) in the host;
- (4) The substituted cation ( $\text{Ca}^{2+}$ ) has ionic radii close to  $\text{Eu}^{2+}$  (see Table 4 below).

The possibilities of Eu abnormal reduction in the  $\beta$ -TCP-type structure can be explained by the following reasons.

The structures of phosphates with the  $\beta$ -TCP type are built from  $\text{PO}_4$  tetrahedra which connect all of the polyhedra by common oxygen atoms into a 3D network. These O atoms are shared by the adjacent polyhedra and tetrahedra and also lined columns A and B in the  $\beta$ - $\text{Ca}_3(\text{PO}_4)_2$  structure. Well chemically bonded O atoms form a rigid structure. This rigid

3D structure of phosphates can shield and isolate the reduced  $\text{Eu}^{2+}$  and  $\text{Mn}^{2+}$  ions from the oxidizing attack of oxygen from the atmosphere.

Second,  $\text{Mn}^{4+}$  may be a luminescent center as well, and its red emission in octahedral sites is due to spin-forbidden  ${}^2\text{E}_g \rightarrow {}^4\text{A}_{2g}$  transitions. However, due to charge imbalance of  $\text{Mn}^{4+}$  and  $\text{Ca}^{2+}$ , for such substitution, the charge compensation scheme in the anionic part is required [42]:



where  $V_{\text{Ca}}$  is a calcium vacancy, and  $[\text{EO}_4]^{4-}$  is an anion with four negative charges, such as  $\text{GeO}_4^{4-}$  or  $\text{SiO}_4^{4-}$ , for instance. Since no charge compensation was applied,  $\text{Mn}^{4+}$  could transfer to the  $\text{Mn}^{2+}$  state, which is more suitable for isovalent substitution. Usually, to stabilize manganese in the +2 oxidation state in the  $\beta$ -TCP hosts,  $\text{MnCO}_3$  is used as a raw material in a reduction atmosphere [13,14,62].

Third, there is a size mismatch between  $\text{Mn}^{4+}$  and  $\text{Ca}^{2+}$  in the  $\beta$ -TCP host. This mismatch can be estimated by the ionic radius percentage difference ( $D_r$ ). For isomorphic substitution, this value could not exceed 30%. The calculation of the ionic radius percentage difference  $D_r$  can be made by the formula:

$$D_r = \frac{|R_h(\text{CN}) - R_d(\text{CN})|}{R_h(\text{CN})}$$

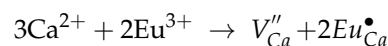
where dopant  $R_d(\text{CN})$  and host  $R_h(\text{CN})$  ions are in the corresponding coordination numbers (CN).  $D_r$  values for different sites in the  $\beta$ -TCP host are given in Table 4. From the above data,  $\text{Mn}^{2+}$  doping into the  $\beta$ -TCP host is more preferable. The absence of emission from  $\text{Mn}^{4+}$  in the octahedra environment (red emission [9,64]) in the studied PL spectra shows its full reduction.

**Table 4.** Calculated  $D_r$  values for Mn and Eu in different oxidation states in the  $\beta$ -TCP host.

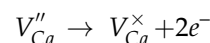
Site	$D_r$ Value, %, for Doped Ion			
	$\text{Mn}^{2+}$	$\text{Mn}^{4+}$	$\text{Eu}^{2+}$	$\text{Eu}^{3+}$
Ca1–Ca3	14	-	11	4
CN8 ( $r = 1.12 \text{ \AA}$ )	( $r = 0.96 \text{ \AA}$ )	-	( $r = 1.25 \text{ \AA}$ )	( $r = 1.07 \text{ \AA}$ )
Ca5	17	47	17	5
CN6 ( $r = 1.00 \text{ \AA}$ )	( $r = 0.83 \text{ \AA}$ )	( $r = 0.53 \text{ \AA}$ )	( $r = 1.17 \text{ \AA}$ )	( $r = 0.95 \text{ \AA}$ )

CN is a coordination number;  $r$  is the ionic radii in the corresponding CN.

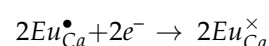
The reduction of  $\text{Eu}^{3+}$  can be explained by a charge compensation model. According to the difference in the oxidation state of  $\text{Ca}^{2+}$  and  $\text{Eu}^{3+}$  ions, two  $\text{Eu}^{3+}$  substitute three  $\text{Ca}^{2+}$  to keep the electroneutrality in the  $\beta$ -TCP host. Hence, one vacancy  $V_{\text{Ca}}''$  with two negative charges locates in the M4 site, while two defects of the cation site  $\text{Eu}_{\text{Ca}}^\bullet$  with a positive charge in each could be produced:



In this substitution,  $V_{\text{Ca}}''$  acts as a donor of electrons, while  $\text{Eu}_{\text{Ca}}^\bullet$  is an acceptor of electrons. Thus, electrons can be transferred from the vacancy as follows during thermal treatment:



and the defect  $\text{Eu}_{\text{Ca}}^\bullet$  captured electrons and further reduced  $\text{Eu}^{3+}$  to  $\text{Eu}^{2+}$ :



A schematic representation of such reduction is present in Figure 16. A similar mechanism was observed in other  $\beta$ -TCP hosts [65] showing that  $\text{Eu}^{3+}$  could not be completely reduced to  $\text{Eu}^{2+}$ , even in the reduction atmosphere due to size mismatching.

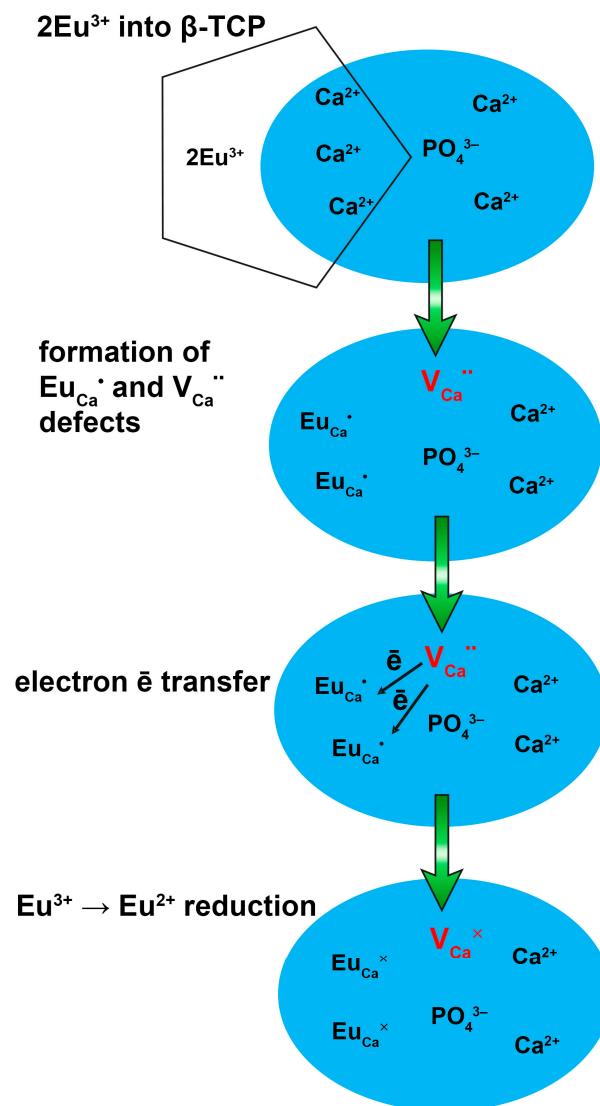
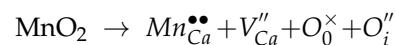
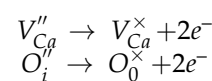


**Figure 16.** The scheme of abnormal reduction of  $\text{Eu}^{3+}$  to  $\text{Eu}^{2+}$  in the  $\beta$ -TCP-type host.

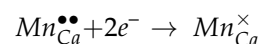
The reduction of  $\text{Mn}^{4+}$  can be described as follows. During thermal treatment, interstitial oxygen  $O_i''$  can be formed due to presence of caves along the  $c$ -axis from  $\text{PO}_4$  frameworks. In order to keep the charge balance, one  $\text{Mn}^{4+}$  is needed to substitute for two  $\text{Ca}^{2+}$  ions. So, one vacancy defect  $V_{Ca}''$  with two negative charges and one  $\text{Mn}_{Ca}^{\bullet\bullet}$  defect with two positive charges would form. Since  $\text{MnO}_2$  is a raw material, these mechanisms can be ascribed by the following:



The cause of the full reduction of  $\text{Mn}^{4+}$  is the possibility of transferring negative charges both from  $V_{Ca}''$  and interstitial oxygen  $O_i''$  during thermal treatment:



So, these electrons would be released to reduce  $\text{Mn}^{4+}$  ions in the  $\text{Ca}^{2+}$  octahedral M5 site:



Such a reduction was previously observed in oxosalt phosphors [66,67].

## 5. Conclusions

Phosphates  $\text{Ca}_{9-x}\text{Mn}_x\text{Eu}(\text{PO}_4)_7$  were obtained by high-temperature solid-phase synthesis. All synthesized samples are isostructural to the  $\beta\text{-Ca}_3(\text{PO}_4)_2$ . Differential scanning calorimetry and dielectric spectroscopy revealed an antiferroelectric first-order reversible phase transition. The structure of  $\text{Ca}_8\text{MnEu}(\text{PO}_4)_7$  was refined by the Rietveld method (sp. gr.  $R\bar{3}c$ ) using synchrotron X-ray diffraction.  $\text{Ca}^{2+}$  and  $\text{Eu}^{3+}$  ions jointly occupy two sites, M1 and M3, while  $\text{Mn}^{2+}$  completely occupies the M5 site. Magnetic measurements have shown that  $\text{Ca}_8\text{MnEu}(\text{PO}_4)_7$  contains  $\text{Mn}^{2+}$  and  $\text{Eu}^{3+}$  ions. XPS data show the coexistence of europium in +3/+2 oxidation states and manganese in the sole +2 oxidation state. The luminescence of  $\text{Eu}^{3+}$  and  $\text{Eu}^{2+}$  ions was found in  $\text{Ca}_{9-x}\text{Mn}_x\text{Eu}(\text{PO}_4)_7$ . The presence of two types of  $\text{Eu}^{2+}/^{3+}$  emission is associated with the partial abnormal self-reduction of europium in the  $\beta\text{-Ca}_3(\text{PO}_4)_2$  matrix. The concentration of  $\text{Eu}^{2+}$  cations is low (~5% according to XPS) and does not affect the magnetic properties. The intensity of  $\text{Eu}^{3+}$  emission is dramatically decreased with the rising of  $\text{Mn}^{2+}$  in  $\text{Ca}_{9-x}\text{Mn}_x\text{Eu}(\text{PO}_4)_7$  and attributed to the  $\text{Eu}^{3+} \rightarrow \text{Mn}^{2+}$  energy transfer. The analysis of the  $^5\text{D}_0 \rightarrow ^7\text{F}_0$  transition and  $R/O$  values points to the symmetry inhomogeneity ( $R3c \rightarrow R\bar{3}c$ ) in  $\text{Ca}_{9-x}\text{Mn}_x\text{Eu}(\text{PO}_4)_7$ , such as in other  $\text{Ca}_{9-x}\text{M}_x\text{Eu}(\text{PO}_4)_7$  solid solutions with divalent metals.

**Supplementary Materials:** The following supporting information can be downloaded at: <https://www.mdpi.com/article/10.3390/ma16041383/s1>, Table S1: Atomic coordinates, displacement parameters ( $\text{\AA}^2$ ) and site-occupancy factors (SOFs) in the structure of  $\text{Ca}_8\text{MnEu}(\text{PO}_4)_7$ ; Table S2: Selected interatomic distances for  $\text{Ca}_8\text{MnEu}(\text{PO}_4)_7$ .

**Author Contributions:** Conceptualization, D.V.D. and V.A.M.; methodology, D.A.S., A.A.B. and V.A.M.; software, E.S.Z. and M.S.M.; validation, E.V.S., N.R.K. and A.A.B.; formal analysis, E.V.S. and N.R.K.; investigation, A.A.B., E.S.Z. and N.R.K.; data curation, D.V.D.; writing—original draft preparation, E.V.S. and D.V.D.; writing—review and editing, D.V.D., N.R.K., D.A.S., V.A.M. and B.I.L.; supervision, D.V.D.; project administration, D.V.D.; funding acquisition, D.V.D. All authors have read and agreed to the published version of the manuscript.

**Funding:** This work was supported by RSF (project 19-77-10013-II). The support of the Estonian Research Council (projects MOBJD613 and PUT PRG111) is also gratefully acknowledged (PL measurements). The study was supported by the Development Program of the Interdisciplinary Scientific and Educational School of Lomonosov Moscow State University's "The future of the planet and global environmental change" and the state assignment of the Chemistry Department of Moscow State University (Agreement No. AAAA-A21-121011590086-0). The X-ray study was carried out in accordance with the state of the Russian Federation, state registration number 122011300125-2. The authors acknowledge support from the Lomonosov Moscow State University Program of Development for providing access to the XPS facility.

**Institutional Review Board Statement:** Not applicable.

**Informed Consent Statement:** Not applicable.

**Data Availability Statement:** Data will be available from the corresponding author on reasonable request.

**Acknowledgments:** The synchrotron radiation experiments were conducted at the former NIMS beamline (BL15XU) of SPring-8 with the approval of the former NIMS Synchrotron X-ray Station (proposal numbers: 2018B4502 and 2020A4501). We thank Y. Katsuya and M. Tanaka for their help at SPring-8. We thank Konstantin I. Maslakov and Serguei V. Savilov for XPS measurements.

**Conflicts of Interest:** The authors declare no conflict of interest.

## References

1. US Department of Energy. Solid State Lighting Research and Development Plan. Available online: [https://energy.gov/sites/prod/files/2016/06/f32/ssl\\_rd-plan\\_%25%0A20jun2016\\_2.pdf](https://energy.gov/sites/prod/files/2016/06/f32/ssl_rd-plan_%25%0A20jun2016_2.pdf) (accessed on 4 January 2023).
2. Lumileds Holding, B.V. Narrow Red Phosphor Technology. Available online: <https://lumileds.com/company/blog/white-paper-narrow-red-phosphor-technology/> (accessed on 4 January 2023).

3. Hu, T.; Ning, L.; Gao, Y.; Qiao, J.; Song, E.; Chen, Z.; Zhou, Y.; Wang, J.; Molokeev, M.S.; Ke, X.; et al. Glass crystallization making red phosphor for high-power warm white lighting. *Light Sci. Appl.* **2021**, *10*, 56. [[CrossRef](#)] [[PubMed](#)]
4. Xie, R.-J.; Li, Y.Q.; Hirosaki, N.; Yamamoto, H. *Nitride Phosphors and Solid-State Lighting*; CRC Press: Boca Raton, FL, USA, 2016; ISBN 9780429103919.
5. Luong, V.D.; Zhang, W.; Lee, H.-R. Preparation of  $\text{Sr}_2\text{Si}_5\text{N}_8:\text{Eu}^{2+}$  for white light-emitting diodes by multi-step heat treatment. *J. Alloys Compd.* **2011**, *509*, 7525–7528. [[CrossRef](#)]
6. Pust, P.; Weiler, V.; Hecht, C.; Tücks, A.; Wochnik, A.S.; Henß, A.-K.; Wiechert, D.; Scheu, C.; Schmidt, P.J.; Schnick, W. Narrow-band red-emitting  $\text{Sr}[\text{LiAl}_3\text{N}_4]:\text{Eu}^{2+}$  as a next-generation LED-phosphor material. *Nat. Mater.* **2014**, *13*, 891–896. [[CrossRef](#)] [[PubMed](#)]
7. Hoerder, G.J.; Seibald, M.; Baumann, D.; Schröder, T.; Peschke, S.; Schmid, P.C.; Tyborski, T.; Pust, P.; Stoll, I.; Bergler, M.; et al.  $\text{Sr}[\text{Li}_2\text{Al}_2\text{O}_2\text{N}_2]:\text{Eu}^{2+}$ —A high performance red phosphor to brighten the future. *Nat. Commun.* **2019**, *10*, 1824. [[CrossRef](#)]
8. Takeda, T.; Xie, R.-J.; Suehiro, T.; Hirosaki, N. Nitride and oxynitride phosphors for white LEDs: Synthesis, new phosphor discovery, crystal structure. *Prog. Solid State Chem.* **2018**, *51*, 41–51. [[CrossRef](#)]
9. Osborne, R.A.; Cherepy, N.J.; Seeley, Z.M.; Payne, S.A.; Drobshoff, A.D.; Srivastava, A.M.; Beers, W.W.; Cohen, W.W.; Schlagel, D.L. New red phosphor ceramic  $\text{K}_2\text{SiF}_6:\text{Mn}^{4+}$ . *Opt. Mater.* **2020**, *107*, 110140. [[CrossRef](#)]
10. Binnemans, K.; Jones, P.T. Rare Earths and the Balance Problem. *J. Sustain. Metall.* **2015**, *1*, 29–38. [[CrossRef](#)]
11. Sinusaite, L.; Renner, A.M.; Schütz, M.B.; Antuzevics, A.; Rogulis, U.; Grigoraviciute-Puroniene, I.; Mathur, S.; Zarkov, A. Effect of Mn doping on the low-temperature synthesis of tricalcium phosphate (TCP) polymorphs. *J. Eur. Ceram. Soc.* **2019**, *39*, 3257–3263. [[CrossRef](#)]
12. Lecointre, A.; Ait Benhamou, R.; Bessiére, A.; Wallez, G.; Elaatmani, M.; Viana, B. Red long-lasting phosphorescence (LLP) in  $\beta$ -TCP type  $\text{Ca}_{9.5}\text{Mn}(\text{PO}_4)_7$  compounds. *Opt. Mater.* **2011**, *34*, 376–380. [[CrossRef](#)]
13. Wang, J.; Shang, M.; Cui, M.; Dang, P.; Liu, D.; Huang, D.; Lian, H.; Lin, J. Realizing an impressive red-emitting  $\text{Ca}_9\text{MnNa}(\text{PO}_4)_7$  phosphor through a dual function based on disturbing structural confinement and energy transfer. *J. Mater. Chem. C* **2020**, *8*, 285–295. [[CrossRef](#)]
14. Liu, W.-R.; Chiu, Y.-C.; Yeh, Y.-T.; Jang, S.-M.; Chen, T.-M. Luminescence and Energy Transfer Mechanism in  $\text{Ca}_{10}\text{K}(\text{PO}_4)_7:\text{Eu}^{2+}, \text{Mn}^{2+}$  Phosphor. *J. Electrochem. Soc.* **2009**, *156*, J165. [[CrossRef](#)]
15. Song, E.; Zhao, W.; Dou, X.; Zhu, Y.; Yi, S.; Min, H. Nonradiative energy transfer from  $\text{Mn}^{2+}$  to  $\text{Eu}^{3+}$  in  $\text{K}_2\text{CaP}_2\text{O}_7:\text{Mn}^{2+}, \text{Eu}^{3+}$  phosphor. *J. Lumin.* **2012**, *132*, 1462–1467. [[CrossRef](#)]
16. Tao, P.; Liu, S.; Wong, W. Phosphorescent Manganese(II) Complexes and Their Emerging Applications. *Adv. Opt. Mater.* **2020**, *8*, 2000985. [[CrossRef](#)]
17. Luo, J.; Zhou, W.; Fan, J.; Sun, Z.; Zhang, X. Composition modification for tuning the luminescent property in  $\text{Sr}_{19}(\text{Mg}, \text{Mn})_2(\text{PO}_4)_{14}:\text{Eu}^{2+}$  phosphors. *J. Lumin.* **2021**, *239*, 118369. [[CrossRef](#)]
18. Cao, R.; Ran, Y.; Lv, X.; Xu, L.; Wan, H.; Hu, Q.; Chen, T.; Cao, C. Tunable multicolor luminescent properties of  $\text{Ca}_8\text{ZnLa}(\text{PO}_4)_7:\text{Ce}^{3+}, \text{Mn}^{2+}$  phosphor via efficient energy transfer. *J. Lumin.* **2019**, *214*, 116549. [[CrossRef](#)]
19. Maciejewska, K.; Poźniak, B.; Tikhomirov, M.; Kobylńska, A.; Marciniak, Ł. Synthesis, Cytotoxicity Assessment and Optical Properties Characterization of Colloidal  $\text{GdPO}_4:\text{Mn}^{2+}, \text{Eu}^{3+}$  for High Sensitivity Luminescent Nanothermometers Operating in the Physiological Temperature Range. *Nanomaterials* **2020**, *10*, 421. [[CrossRef](#)]
20. Félix-Quintero, H.; Falcony, C.; Hernández, A.J.; Camarillo, G.E.; Flores, J.C.; Murrieta, S.H.  $\text{Mn}^{2+}$  to  $\text{Eu}^{3+}$  energy transfer in zinc phosphate glass. *J. Lumin.* **2020**, *225*, 117337. [[CrossRef](#)]
21. Chen, Y.; Li, Y.; Wang, J.; Wu, M.; Wang, C. Color-Tunable Phosphor of  $\text{Eu}^{2+}$  and  $\text{Mn}^{2+}$  Codoped  $\text{Ca}_2\text{Sr}(\text{PO}_4)_2$  for UV Light-Emitting Diodes. *J. Phys. Chem. C* **2014**, *118*, 12494–12499. [[CrossRef](#)]
22. Zhang, J.; Zhai, Z.; Hua, Z. Investigations on luminescence of  $\text{Ca}_8\text{MgGd}(\text{PO}_4)_7:\text{Eu}^{2+}, \text{Mn}^{2+}, \text{Yb}^{3+}, \text{Er}^{3+}, \text{Ho}^{3+}, \text{Tm}^{3+}$  phosphors. *Mater. Res. Bull.* **2016**, *74*, 34–40. [[CrossRef](#)]
23. Belik, A.A.; Gutan, V.B.; Ivanov, L.N.; Lazoryak, B.I. Synthesis, structure, and luminescence properties of  $\text{Ca}_9\text{MnM}(\text{PO}_4)_7$  ( $\text{M} = \text{Li}, \text{Na}, \text{K}$ ). *Russ. J. Inorg. Chem.* **2001**, *46*, 785–792.
24. Kang, X.; Lü, W.; Wang, H.; Ling, D. Energy Transfer from  $\text{Ce}^{3+}$  to  $\text{Tb}^{3+}/\text{Dy}^{3+}/\text{Mn}^{2+}$  in  $\text{Ca}_9\text{Ga}(\text{PO}_4)_7$  Phosphors: Synthesis, Structure and Tunable Multicolor Luminescent Properties. *ChemPhysChem* **2019**, *20*, 861–867. [[CrossRef](#)] [[PubMed](#)]
25. Guo, N.; Li, S.; Chen, J.; Li, J.; Zhao, Y.; Wang, L.; Jia, C.; Ouyang, R.; Lü, W. Photoluminescence properties of whitlockite-type  $\text{Ca}_9\text{MgK}(\text{PO}_4)_7:\text{Eu}^{2+}, \text{Mn}^{2+}$  phosphor. *J. Lumin.* **2016**, *179*, 328–333. [[CrossRef](#)]
26. Ding, C.; Tang, W. Crystal structure, energy transfer and tunable luminescence properties of  $\text{Ca}_8\text{ZnCe}(\text{PO}_4)_7:\text{Eu}^{2+}, \text{Mn}^{2+}$  phosphor. *Opt. Mater.* **2018**, *76*, 56–62. [[CrossRef](#)]
27. Rietveld, H.M. A profile refinement method for nuclear and magnetic structures. *J. Appl. Crystallogr.* **1969**, *2*, 65–71. [[CrossRef](#)]
28. Petricek, V.; Dusek, M.; Palatinus, L.; Petricek, V.; Dušek, M.; Palatinus, L. Crystallographic computing system JANA2006: General features. *Z. Krist.* **2014**, *229*, 345–352. [[CrossRef](#)]
29. Deyneko, D.V.; Aksenov, S.M.; Nikiforov, I.; Stefanovich, S.Y.; Lazoryak, B.I. Symmetry Inhomogeneity of  $\text{Ca}_{9-x}\text{Zn}_x\text{Eu}(\text{PO}_4)_7$  Phosphor Determined by Second-Harmonic Generation and Dielectric and Photoluminescence Spectroscopy. *Cryst. Growth Des.* **2020**, *20*, 6461–6468. [[CrossRef](#)]
30. Nikiforov, I.V.; Deyneko, D.V.; Spassky, D.A.; Baryshnikova, O.V.; Stefanovich, S.Y.; Lazoryak, B.I. Tunable luminescence and energy transfer in  $\text{Eu}^{3+}$  doped  $\text{Ca}_8\text{MTb}(\text{PO}_4)_7$  ( $\text{M} = \text{Mg}, \text{Zn}, \text{Ca}$ ) phosphors. *Mater. Res. Bull.* **2020**, *130*, 110925. [[CrossRef](#)]

31. Deyneko, D.V.; Morozov, V.A.; Zhukovskaya, E.S.; Nikiforov, I.V.; Spassky, D.A.; Belik, A.A.; Lazoryak, B.I. The influence of second coordination-sphere interactions on the luminescent properties of  $\beta$ -Ca<sub>3</sub>(PO<sub>4</sub>)<sub>2</sub>-related compounds. *J. Alloys Compd.* **2020**, *815*, 152352. [[CrossRef](#)]
32. Nikiforov, I.V.; Deyneko, D.V.; Duskaev, I.F. Structural Features of Phosphates Ca<sub>9-x</sub>M<sub>x</sub>Dy(PO<sub>4</sub>)<sub>7</sub> (M = Zn<sup>2+</sup> or Mg<sup>2+</sup>). *Phys. Solid State* **2020**, *62*, 860–864. [[CrossRef](#)]
33. Deyneko, D.V.; Nikiforov, I.V.; Spassky, D.A.; Dikhtyar, Y.Y.; Aksenov, S.M.; Stefanovich, S.Y.; Lazoryak, B.I. Luminescence of Eu<sup>3+</sup> as a probe for the determination of the local site symmetry in  $\beta$ -Ca<sub>3</sub>(PO<sub>4</sub>)<sub>2</sub>-related structures. *CrystEngComm* **2019**, *21*, 5235–5242. [[CrossRef](#)]
34. Deyneko, D.V.; Morozov, V.A.; Vasin, A.A.; Aksenov, S.M.; Dikhtyar, Y.Y.; Stefanovich, S.Y.; Lazoryak, B.I. The crystal site engineering and turning of cross-relaxation in green-emitting  $\beta$ -Ca<sub>3</sub>(PO<sub>4</sub>)<sub>2</sub>-related phosphors. *J. Lumin.* **2020**, *223*, 117196. [[CrossRef](#)]
35. Dikhtyar, Y.Y.; Deyneko, D.V.; Boldyrev, K.N.; Baryshnikova, O.V.; Belik, A.A.; Morozov, V.A.; Lazoryak, B.I. Crystal structure, dielectric and optical properties of  $\beta$ -Ca<sub>3</sub>(PO<sub>4</sub>)<sub>2</sub>-type phosphates Ca<sub>9-x</sub>Zn<sub>x</sub>La(PO<sub>4</sub>)<sub>7</sub>:Ho<sup>3+</sup>. *J. Lumin.* **2021**, *236*, 118083. [[CrossRef](#)]
36. Dikhtyar, Y.Y.; Deyneko, D.V.; Spassky, D.A.; Lazoryak, B.I.; Stefanovich, S.Y. A novel high color purity blue-emitting Tm<sup>3+</sup>-doped  $\beta$ -Ca<sub>3</sub>(PO<sub>4</sub>)<sub>2</sub>-type phosphor for WLED application. *Optik* **2020**, *227*, 166027. [[CrossRef](#)]
37. Belik, A.A.; Morozov, V.A.; Deyneko, D.V.; Savon, A.E.; Baryshnikova, O.V.; Zhukovskaya, E.S.; Dorbakov, N.G.; Katsuya, Y.; Tanaka, M.; Stefanovich, S.Y.; et al. Antiferroelectric properties and site occupations of R<sup>3+</sup> cations in Ca<sub>8</sub>MgR(PO<sub>4</sub>)<sub>7</sub> luminescent host materials. *J. Alloys Compd.* **2017**, *699*, 928–937. [[CrossRef](#)]
38. Lazoryak, B.I.; Zhukovskaya, E.S.; Baryshnikova, O.V.; Belik, A.A.; Leonidova, O.N.; Deyneko, D.V.; Savon, A.E.; Dorbakov, N.G.; Morozov, V.A. Luminescence, structure and antiferroelectric-type phase transition in Ca<sub>8</sub>ZnEu(PO<sub>4</sub>)<sub>7</sub>. *Mater. Res. Bull.* **2018**, *104*, 20–26. [[CrossRef](#)]
39. Dikhtyar, Y.Y.; Spassky, D.A.; Morozov, V.A.; Deyneko, D.V.; Belik, A.A.; Baryshnikova, O.V.; Nikiforov, I.V.; Lazoryak, B.I. Site occupancy, luminescence and dielectric properties of  $\beta$ -Ca<sub>3</sub>(PO<sub>4</sub>)<sub>2</sub>-type Ca<sub>8</sub>ZnLn(PO<sub>4</sub>)<sub>7</sub> host materials. *J. Alloys Compd.* **2022**, *908*, 164521. [[CrossRef](#)]
40. Stefanovich, S.Y.; Petrova, D.A.; Morozov, V.A.; Fortalnova, E.A.; Belov, D.A.; Deyneko, D.V.; Lazoryak, B.I. Enhanced nonlinear optical activity and Ca<sup>2+</sup>-conductivity in Ca<sub>10.5-x</sub>Pb<sub>x</sub>(VO<sub>4</sub>)<sub>7</sub> ferroelectrics. *J. Alloys Compd.* **2018**, *735*, 1826–1837.
41. Altomare, A.; Rizzi, R.; Rossi, M.; El Khouri, A.; Elaati, M.; Paterlini, V.; Della Ventura, G.; Capitelli, F. New Ca<sub>2.90</sub>(Me<sup>2+</sup>)<sub>0.10</sub>(PO<sub>4</sub>)<sub>2</sub>  $\beta$ -tricalcium Phosphates with Me<sup>2+</sup> = Mn, Ni, Cu: Synthesis, Crystal-Chemistry, and Luminescence Properties. *Crystals* **2019**, *9*, 288. [[CrossRef](#)]
42. Deyneko, D.V.; Nikiforov, I.V.; Lazoryak, B.I.; Aksenov, S.M. The role of anionic heterovalent [PO<sub>4</sub>]<sup>3-</sup> → [GeO<sub>4</sub>]<sup>4-</sup> substitution on the luminescence properties of inorganic phosphors with the  $\beta$ -Ca<sub>3</sub>(PO<sub>4</sub>)<sub>2</sub>-type structure: New data based on accurate crystal structure refinement. *Dalt. Trans.* **2022**, *51*, 655–663. [[CrossRef](#)]
43. Deyneko, D.V.; Titkov, V.V.; Fedyunin, F.D.; Spassky, D.A.; Volkov, S.N.; Borovikova, E.Y.; Lazoryak, B.I.; Aksenov, S.M. «Ellestadite»-type anionic [PO<sub>4</sub>]<sup>3-</sup> → [SO<sub>4</sub>]<sup>2-</sup> substitutions in  $\beta$ -Ca<sub>3</sub>(PO<sub>4</sub>)<sub>2</sub> type compounds: A new route to design the inorganic phosphors. *Ceram. Int.* **2022**, *48*, 24012–24020. [[CrossRef](#)]
44. Kittel, C. *Introduction to Solid State Physics*, 8th ed.; John Wiley and Sons: New York, NY, USA, 2005.
45. Baltrus, J.P.; Keller, M.J. Rare earth oxides Eu<sub>2</sub>O<sub>3</sub> and Nd<sub>2</sub>O<sub>3</sub> analyzed by XPS. *Surf. Sci. Spectra* **2019**, *26*, 014001. [[CrossRef](#)]
46. Kumar, S.; Prakash, R.; Choudhary, R.J.; Phase, D.M. Structural, XPS and magnetic studies of pulsed laser deposited Fe doped Eu<sub>2</sub>O<sub>3</sub> thin film. *Mater. Res. Bull.* **2015**, *70*, 392–396. [[CrossRef](#)]
47. Shin, Y.C.; Leem, S.J.; Kim, C.M.; Kim, S.J.; Sung, Y.M.; Hahn, C.K.; Baek, J.H.; Kim, T.G. Deposition of Europium Oxide on Si and its optical properties depending on thermal annealing conditions. *J. Electroceramics* **2009**, *23*, 326–330. [[CrossRef](#)]
48. Vercaemst, R.; Poelman, D.; Fiermans, L.; Van Meirhaeghe, R.L.; Laflère, W.H.; Cardon, F. A detailed XPS study of the rare earth compounds EuS and EuF<sub>3</sub>. *J. Electron Spectros. Relat. Phenom.* **1995**, *74*, 45–56. [[CrossRef](#)]
49. Schneider, W.-D.; Laubschat, C.; Nowik, I.; Kaindl, G. Shake-up excitations and core-hole screening in Eu systems. *Phys. Rev. B* **1981**, *24*, 5422–5425. [[CrossRef](#)]
50. Kang, J.-G.; Jung, Y.; Min, B.-K.; Sohn, Y. Full characterization of Eu(OH)<sub>3</sub> and Eu<sub>2</sub>O<sub>3</sub> nanorods. *Appl. Surf. Sci.* **2014**, *314*, 158–165. [[CrossRef](#)]
51. Mercier, F.; Alliot, C.; Bion, L.; Thromat, N.; Toulhoat, P. XPS study of Eu(III) coordination compounds: Core levels binding energies in solid mixed-oxo-compounds Eu<sub>m</sub>X<sub>x</sub>O<sub>y</sub>. *J. Electron Spectros. Relat. Phenom.* **2006**, *150*, 21–26. [[CrossRef](#)]
52. Ilton, E.S.; Post, J.E.; Heaney, P.J.; Ling, F.T.; Kerisit, S.N. XPS determination of Mn oxidation states in Mn (hydr)oxides. *Appl. Surf. Sci.* **2016**, *366*, 475–485. [[CrossRef](#)]
53. Langell, M.; Hutchings, C.W.; Carson, G.A.; Nassir, M.H. High resolution electron energy loss spectroscopy of MnO(100) and oxidized MnO(100). *J. Vac. Sci. Technol. A* **1996**, *14*, 1656–1661. [[CrossRef](#)]
54. Soares, E.A.; Paniago, R.; de Carvalho, V.E.; Lopes, E.L.; Abreu, G.J.P.; Pfannes, H.-D. Quantitative low-energy electron diffraction analysis of MnO(00) films grown on Ag(100). *Phys. Rev. B* **2006**, *73*, 035419. [[CrossRef](#)]
55. Stranick, M.A. Mn<sub>2</sub>O<sub>3</sub> by XPS. *Surf. Sci. Spectra* **1999**, *6*, 39–46. [[CrossRef](#)]
56. Stranick, M.A. MnO<sub>2</sub> by XPS. *Surf. Sci. Spectra* **1999**, *6*, 31–38. [[CrossRef](#)]
57. Zhao, M.; Zhang, Q.; Xia, Z. Structural Engineering of Eu<sup>2+</sup>-Doped Silicates Phosphors for LED Applications. *Acc. Mater. Res.* **2020**, *1*, 137–145. [[CrossRef](#)]

58. Zhang, H.; Lü, M.; Xiu, Z.; Wang, S.; Zhou, G.; Zhou, Y.; Wang, S.; Qiu, Z.; Zhang, A. Synthesis and photoluminescence properties of a new red emitting phosphor:  $\text{Ca}_3(\text{VO}_4)_2:\text{Eu}^{3+}; \text{Mn}^{2+}$ . *Mater. Res. Bull.* **2007**, *42*, 1145–1152. [[CrossRef](#)]
59. Dai, W.B. Mechanism of the reduction and energy transfer between  $\text{Eu}^{2+}$  and  $\text{Eu}^{3+}$  in Eu-doped  $\text{CaAl}_2\text{Si}_2\text{O}_8$  materials prepared in air. *J. Mater. Chem. C* **2014**, *2*, 3951–3959. [[CrossRef](#)]
60. Chen, J.; Liang, Y.; Zhu, Y.; Liu, S.; Li, H.; Lei, W. Abnormal reduction of  $\text{Eu}^{3+}$  to  $\text{Eu}^{2+}$  in  $\text{Sr}_5(\text{PO}_4)_3\text{Cl}:\text{Eu}$  phosphor and its enhanced red emission by the charge compensation. *J. Lumin.* **2019**, *214*, 116569. [[CrossRef](#)]
61. Li, H.; Wang, Y. Effect of Oxygen Vacancies on the Reduction of  $\text{Eu}^{3+}$  in  $\text{Mg}_3\text{Ca}_3(\text{PO}_4)_4$  in Air Atmosphere. *Inorg. Chem.* **2017**, *56*, 10396–10403. [[CrossRef](#)]
62. Dang, P.; Liu, D.; Li, G.; Liang, S.; Lian, H.; Shang, M.; Lin, J. Mixing the valence control of  $\text{Eu}^{2+}/\text{Eu}^{3+}$  and energy transfer construction of  $\text{Eu}^{2+}/\text{Mn}^{2+}$  in the solid solution  $(1-x)\text{Ca}_3(\text{PO}_4)_2-x\text{Ca}_9\text{Y}(\text{PO}_4)_7$  for multichannel photoluminescence tuning. *Inorg. Chem. Front.* **2019**, *6*, 2837–2849. [[CrossRef](#)]
63. Peng, M.; Pei, Z.; Hong, G.; Su, Q. The reduction of  $\text{Eu}^{3+}$  to  $\text{Eu}^{2+}$  in  $\text{BaMgSiO}_4:\text{Eu}$  prepared in air and the luminescence of  $\text{BaMgSiO}_4:\text{Eu}^{2+}$  phosphor. *J. Mater. Chem.* **2003**, *13*, 1202–1205. [[CrossRef](#)]
64. Xu, W.; Chen, D.; Yuan, S.; Zhou, Y.; Li, S. Tuning excitation and emission of  $\text{Mn}^{4+}$  emitting center in  $\text{Y}_3\text{Al}_5\text{O}_{12}$  by cation substitution. *Chem. Eng. J.* **2017**, *317*, 854–861. [[CrossRef](#)]
65. Yu, H.; Ruan, F.; Chen, L.; Deng, D. Dual-emitting  $\text{Eu}^{2+}/\text{Eu}^{3+}$  co-doped  $\text{Ca}_9\text{Zn}_{1.5}(\text{PO}_4)_7$  phosphor for self-calibrated optical thermometry. *Opt. Mater.* **2020**, *100*, 109678. [[CrossRef](#)]
66. Lu, J.; Pan, Y.; Wang, J.; Chen, X.; Huang, S.; Liu, G. Reduction of  $\text{Mn}^{4+}$  to  $\text{Mn}^{2+}$  in  $\text{CaAl}_{12}\text{O}_{19}$  by co-doping charge compensators to obtain tunable photoluminescence. *RSC Adv.* **2013**, *3*, 4510–4513. [[CrossRef](#)]
67. Hu, J.Q.; Song, E.H.; Ye, S.; Zhou, B.; Zhang, Q.Y. Anomalous spontaneous-reduction of  $\text{Mn}^{7+}/\text{Mn}^{4+}$  to  $\text{Mn}^{2+}$  and luminescence properties in  $\text{Zn}_2\text{GeO}_4:\text{Mn}$ . *J. Mater. Chem. C* **2017**, *5*, 3343–3351. [[CrossRef](#)]

**Disclaimer/Publisher's Note:** The statements, opinions and data contained in all publications are solely those of the individual author(s) and contributor(s) and not of MDPI and/or the editor(s). MDPI and/or the editor(s) disclaim responsibility for any injury to people or property resulting from any ideas, methods, instructions or products referred to in the content.